





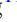











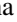





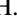









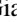
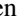






# CSS 161010: A Luminous Fast Blue Optical Transient with Broad Blueshifted Hydrogen Lines

Claudia P. Gutiérrez<sup>1,2,3,4</sup> , Seppo Mattila<sup>4,5</sup> , Peter Lundqvist<sup>6</sup> , Luc Dessart<sup>7</sup> , Santiago González-Gaitán<sup>8</sup> , Peter G. Jonker<sup>9,10</sup> , Subo Dong<sup>11,12,13</sup> , Deanne Coppejans<sup>14</sup> , Ping Chen<sup>11,15</sup>, Panos Charalampopoulos<sup>4</sup> , Nancy Elias-Rosa<sup>16,2</sup> , Thomas M. Reynolds<sup>4,17,18</sup> , Christopher Kochanek<sup>19,20</sup> , Morgan Fraser<sup>21</sup> , Andrea Pastorello<sup>16</sup> , Mariusz Gromadzki<sup>22</sup> , Jack Neustadt<sup>19,20</sup> , Stefano Benetti<sup>16</sup> , Erkki Kankare<sup>4</sup> , Tuomas Kangas<sup>3,4</sup> , Rubina Kotak<sup>4</sup> , Maximilian D. Stritzinger<sup>23</sup> , Thomas Wevers<sup>24,25</sup> , Bing Zhang<sup>26,27</sup> , David Bersier<sup>28</sup>, Subhash Bose<sup>23</sup> , David A. H. Buckley<sup>29,30,31</sup> , Raya Dastidar<sup>32,33</sup> , Anjasha Gangopadhyay<sup>34</sup> , Aleksandra Hamanowicz<sup>24</sup> , Juna A. Kollmeier<sup>35,36</sup>, Jirong Mao<sup>37</sup> , Kuntal Misra<sup>38</sup> , Stephen. B. Potter<sup>29,39</sup> , Jose L. Prieto<sup>32,40</sup> , Encarni Romero-Colmenero<sup>29,41</sup> , Mridweeka Singh<sup>42</sup> , Auni Somero<sup>4</sup> , Giacomo Terreran<sup>43,44</sup> , Petri Vaisanen<sup>3,29</sup> , and Łukasz Wyrzykowski<sup>22</sup> 

<sup>1</sup> Institut d'Estudis Espacials de Catalunya (IEEC), Edifici RDIT, Campus UPC, 08860 Castelldefels (Barcelona), Spain; [cgutierrez@ice.csic.es](mailto:cgutierrez@ice.csic.es)

<sup>2</sup> Institute of Space Sciences (ICE, CSIC), Campus UAB, Carrer de Can Magrans, s/n, E-08193 Barcelona, Spain

<sup>3</sup> Finnish Centre for Astronomy with ESO (FINCA), FI-20014, University of Turku, Finland

<sup>4</sup> Department of Physics and Astronomy, FI-20014, University of Turku, Finland

<sup>5</sup> School of Sciences, European University Cyprus, Diogenes Street, Engomi, 1516 Nicosia, Cyprus

<sup>6</sup> The Oskar Klein Centre, Department of Astronomy, Stockholm University, AlbaNova, SE-10691, Stockholm, Sweden

<sup>7</sup> Institut d'Astrophysique de Paris, CNRS-Sorbonne Université, 98 bis boulevard Arago, F-75014 Paris, France

<sup>8</sup> CENTRA, Instituto Superior Técnico, Universidade de Lisboa, Av. Rovisco Pais 1, 1049-001 Lisboa, Portugal

<sup>9</sup> Department of Astrophysics/IMAPP, Radboud University, P.O. Box 9010, 6500 GL Nijmegen, The Netherlands

<sup>10</sup> SRON, Netherlands Institute for Space Research, Niels Bohrweg 4, 2333 CA, Leiden, The Netherlands

<sup>11</sup> Department of Astronomy, School of Physics, Peking University, 5 Yiheyuan Road, Haidian District, Beijing 100871, People's Republic of China

<sup>12</sup> Kavli Institute of Astronomy and Astrophysics, Peking University, 5 Yiheyuan Road, Haidian District, Beijing 100871, People's Republic of China

<sup>13</sup> National Astronomical Observatories, Chinese Academy of Science, 20A Datun Road, Chaoyang District, Beijing 100101, People's Republic of China

<sup>14</sup> Department of Physics, University of Warwick, Gibbet Hill Road, Coventry CV4 7AL, UK

<sup>15</sup> Department of Particle Physics and Astrophysics, Weizmann Institute of Science, 234 Herzl St, 76100 Rehovot, Israel

<sup>16</sup> INAF—Osservatorio Astronomico di Padova, Vicolo dell'Osservatorio 5, Padova I-35122, Italy

<sup>17</sup> Cosmic Dawn Center (DAWN)

<sup>18</sup> Niels Bohr Institute, University of Copenhagen, Jagtvej 128, DK-2200, Copenhagen N, Denmark

<sup>19</sup> Department of Astronomy, The Ohio State University, 140 West 18th Avenue, Columbus, OH 43210, USA

<sup>20</sup> Center for Cosmology and AstroParticle Physics, The Ohio State University, 191 West Woodruff Avenue, Columbus, OH 43210, USA

<sup>21</sup> UCD School of Physics, L.M.I. Main Building, Beech Hill Road, Dublin 4, D04 P7W1, Ireland

<sup>22</sup> Astronomical Observatory, University of Warsaw, Al. Ujazdowskie 4, 00-478 Warszawa, Poland

<sup>23</sup> Department of Physics and Astronomy, Aarhus University, Ny Munkegade 120, DK-8000 Aarhus C, Denmark

<sup>24</sup> Space Telescope Science Institute, 3700 San Martin Drive, Baltimore, MD 21218, USA

<sup>25</sup> European Southern Observatory, Alonso de Córdova 3107, Vitacura, Santiago, Chile

<sup>26</sup> Nevada Center for Astrophysics, University of Nevada, Las Vegas, 4505 South Maryland Parkway, Las Vegas, NV 89154, USA

<sup>27</sup> Department of Physics and Astronomy, University of Nevada, Las Vegas, 4505 South Maryland Parkway, Las Vegas, NV 89154, USA

<sup>28</sup> Astrophysics Research Institute, Liverpool Science Park IC2, Liverpool L3 5RF, UK

<sup>29</sup> South African Astronomical Observatory, P.O. Box 9, Observatory, 7935 Cape Town, South Africa

<sup>30</sup> Department of Astronomy, University of Cape Town, Private Bag X3, 7701 Rondebosch, South Africa

<sup>31</sup> Department of Physics, University of the Free State, P.O. Box 339, 9300 Bloemfontein, South Africa

<sup>32</sup> Millennium Institute of Astrophysics MAS, Nuncio Monseñor Sotero Sanz 100, Providencia, Santiago, 8320000, Chile

<sup>33</sup> Instituto de Astrofísica, Universidad Andres Bello, Fernandez Concha 700, Las Condes, Santiago, Chile

<sup>34</sup> Oskar Klein Centre, Department of Astronomy, Stockholm University, Albanova University Centre, SE-106 91 Stockholm, Sweden

<sup>35</sup> The Observatories of the Carnegie Institution for Science, 813 Santa Barbara Street, Pasadena, CA 91101, USA

<sup>36</sup> Canadian Institute for Theoretical Astrophysics, University of Toronto, Toronto, ON M5S 98H, Canada

<sup>37</sup> Yunnan Observatories, Chinese Academy of Science, 650011 Kunming, Yunnan Province, People's Republic of China

<sup>38</sup> Aryabhata Research Institute of Observational Sciences, Nainital-263001, India

<sup>39</sup> Department of Physics, University of Johannesburg, P.O. Box 524, 2006 Auckland Park, South Africa

<sup>40</sup> Instituto de Estudios Astrofísicos, Facultad de Ingeniería y Ciencias, Universidad Diego Portales, Av. Ejército Libertador 441, Santiago, Chile

<sup>41</sup> Southern African Large Telescope (SALT), P.O. Box 9, Observatory, 7935 Cape Town, South Africa

<sup>42</sup> Indian Institute of Astrophysics, Koramangala 2nd Block, Bangalore 560034, India

<sup>43</sup> Las Cumbres Observatory, 6740 Cortona Drive, Suite 102, Goleta, CA 93117-5575, USA

<sup>44</sup> Department of Physics, University of California, Santa Barbara, CA 93106-9530, USA

Received 2024 August 7; revised 2024 October 10; accepted 2024 October 14; published 2024 December 11

## Abstract

We present ultraviolet, optical, and near-infrared photometric and optical spectroscopic observations of the luminous fast blue optical transient (LFBOT) CSS 161010:045834–081803 (CSS 161010). The transient was found in a low-redshift ( $z = 0.033$ ) dwarf galaxy. The light curves of CSS 161010 are characterized by an extremely fast evolution

and blue colors. The  $V$ -band light curve shows that CSS 161010 reaches an absolute peak of  $M_V^{\max} = -20.66 \pm 0.06$  mag in 3.8 days from the start of the outburst. After maximum, CSS 161010 follows a power-law decline  $\propto t^{-2.8 \pm 0.1}$  in all optical bands. These photometric properties are comparable to those of well-observed LFBOTs such as AT 2018cow, AT 2020mrf, and AT 2020xnd. However, unlike these objects, the spectra of CSS 161010 show a remarkable transformation from a blue and featureless continuum to spectra dominated by very broad, entirely blueshifted hydrogen emission lines with velocities of up to 10% of the speed of light. The persistent blueshifted emission and the lack of any emission at the rest wavelength of CSS 161010 are unique features not seen in any transient before CSS 161010. The combined observational properties of CSS 161010 and its  $M_* \sim 10^8 M_\odot$  dwarf galaxy host favor the tidal disruption of a star by an intermediate-mass black hole as its origin.

*Unified Astronomy Thesaurus concepts:* [Transient sources \(1851\)](#); [Supernovae \(1668\)](#)

## 1. Introduction

High-cadence, wide-field sky surveys have revealed a significant number of new extragalactic transients that show a large diversity in their spectral and photometric behavior. Among the new types of objects, one group attracts attention due to their remarkably rapid evolution: the fast blue optical transients (FBOTs; M. R. Drout et al. 2014; M. Pursiainen et al. 2018; C. Inerra 2019) or fast-evolving luminous transients (FELTs; A. Rest et al. 2018). FBOTs are characterized by rise times of  $< 10$  days, peak absolute magnitudes of  $-15 \text{ mag} > M_g^{\max} > -22 \text{ mag}$ , and blue colors. Their hosts are generally found to be low-mass star-forming galaxies (M. R. Drout et al. 2014; M. Pursiainen et al. 2018). Due to their fast evolution, they are difficult to explain as supernovae (SNe) powered by the radioactive decay of  $^{56}\text{Ni}$  (M. R. Drout et al. 2014). Multiple different scenarios have been proposed to explain their properties, including shock breakout emission within a dense surrounding wind or shell (e.g., E. O. Ofek et al. 2010; M. R. Drout et al. 2014; A. Rest et al. 2018), cooling envelope emission from the explosion of a star with a low-mass extended envelope with very little radioactive material (M. R. Drout et al. 2014), a common envelope jet (N. Soker et al. 2019; N. Soker 2022), a tidal disruption event (TDE) caused by an intermediate-mass black hole (IMBH; D. A. Perley et al. 2019), and fallback accretion (R. Margutti et al. 2019).

Most FBOTs have been found in archival data from large imaging surveys, such as Pan-STARRS1<sup>45</sup> (PS1; M. R. Drout et al. 2014), the Palomar Transient Factory, the Supernova Legacy Survey (I. Arcavi et al. 2016), and the Dark Energy Survey (M. Pursiainen et al. 2018; P. Wiseman et al. 2020) as well as from observations by the Kepler space telescope (A. Rest et al. 2018). However, this picture is changing thanks to surveys that monitor the sky with a cadence of a few days (e.g., the All-Sky Automated Survey for SuperNovae, ASAS-SN, B. J. Shappee et al. 2014; the Asteroid Terrestrial-impact Last Alert System, ATLAS, J. L. Tonry et al. 2018; K. W. Smith et al. 2020; and the Zwicky Transient Facility, E. C. Bellm et al. 2019; M. J. Graham et al. 2019), and new efforts focus on finding and characterizing these events in almost real time (e.g., D. A. Perley et al. 2021; A. Y. Q. Ho et al. 2023b).

After the discovery of AT 2018cow (S. J. Prentice et al. 2018; A. Y. Q. Ho et al. 2019; R. Margutti et al. 2019; D. A. Perley et al. 2019; Y. Chen et al. 2023; A. Inkenhaag et al. 2023), a new luminous subclass of FBOTs, now known as luminous FBOTs (LFBOTs), was identified. This class includes AT 2018lug (ZTF18abvkwla; A. Y. Q. Ho et al. 2020), CRTS-

CSS 161010 J045834–081803 (CSS 161010D, L. Coppejans et al. 2020, hereafter C20), AT 2020xnd (D. A. Perley et al. 2021; J. S. Bright et al. 2022; A. Y. Q. Ho et al. 2022), AT 2020mrf (Y. Yao et al. 2022), AT 2022tsd (A. Y. Q. Ho et al. 2023a; D. Matthews et al. 2023), and AT 2023fhn (A. A. Chrimes et al. 2024a, 2024b). Most of these objects have been detected in the optical, radio, and X-rays. The only exception was AT 2018lug, which had no X-ray observations. Unlike in optical photometry, where all the objects follow a similar evolution, their behavior is more diverse in the radio and X-rays: AT 2018lug is the most luminous of these events in the radio, while AT 2022tsd is the most luminous in the X-rays. Unfortunately, due to their fast evolution, multiepoch spectral coverage in the optical has been scarce and consists of featureless spectra, except for AT 2018cow. Therefore, despite extensive observations in different wavelengths, their nature is debated, and their origin is still unknown. However, recent observations of AT 2018cow at late epochs suggest that a central engine (D. R. Pasham et al. 2021) in the form of a black hole (BH) must be present (A. Inkenhaag et al. 2023), although it is unclear whether it is a stellar-mass BH or an IMBH (G. Migliori et al. 2024).

Although these LFBOTs were first detected, identified, and analyzed in the optical, CSS 161010 has only been characterized in the radio and X-rays (C20). We present the first ultraviolet (UV), optical, and near-infrared (NIR) observations of CSS 161010. The remarkable spectral and photometric coverage allows us to study its properties in detail. In particular, the detection of broad, entirely blueshifted hydrogen lines and the available information in the X-ray and radio (C20) may help us to provide important insights into these fast events.

The paper is organized as follows. A brief description of the observations is presented in Section 2. Section 3 characterizes and discusses the nature of CSS 161010. In Section 3.6, we discuss the origin of CSS 161010, while our summary is given in Section 4. Throughout this work, we assume a flat  $\Lambda$ CDM Universe, with a Hubble constant of  $H_0 = 70 \text{ km s}^{-1} \text{ Mpc}^{-1}$  and  $\Omega_m = 0.3$ .

## 2. Observations of CSS 161010

CSS 161010 (R.A. =  $04^{\text{h}}58^{\text{m}}34^{\text{s}}.41$ , decl. =  $-08^{\circ}18'03''.5$ , J2000) was discovered by the Catalina Real-Time Transient Survey (A. J. Drake et al. 2009) on 2016 October 10 (JD = 2457671.98) at an unfiltered apparent magnitude of 16.29. An earlier detection was obtained by ASAS-SN (B. J. Shappee et al. 2014) on JD = 2457671.70 at an apparent  $V$ -band magnitude of  $16.51 \pm 0.12$  mag. The last nondetection obtained by ASAS-SN was on 2016 October 6 (JD = 2457667.78; detection limit of  $m_V \sim 17.54$  mag). ATLAS obtained the deepest and latest nondetection on 2016 October 6 (JD = 2457668.14; detection

<sup>45</sup> <https://catalogs.mast.stsci.edu/panstarrs/>

limit of  $m_c \sim 19.59$  mag). We adopt the midpoint between ATLAS’s last nondetection and ASAS-SN’s first detection as the start of the outburst epoch,  $\text{JD} = 2457669.92 \pm 2.00$ .

CSS 161010 was spectroscopically observed on 2016 October 18 (T. Reynolds et al. 2016) and reported as a blue and nearly featureless object. Given its nuclear location, fast photometric evolution, and blue featureless spectrum, we started our follow-up on this date ( $\sim 9$  days from the start of the outburst). A total of 12 epochs of optical spectroscopy were obtained from 9.4 to 106.0 days with five different instruments, while multiwavelength photometric coverage was obtained between 1.72 and 77.91 days. The observations and data reduction details are presented in Appendix A.

### 3. Analysis of CSS 161010

#### 3.1. Galaxy

The host galaxy of CSS 161010 is WISEA J045834.37–081804.4 (Figure 1), a dwarf galaxy ( $M_V = -14.7$  mag) at  $z = 0.0340 \pm 0.0006$  (i.e., luminosity distance  $D_L = 149.4$  Mpc or a distance modulus of  $\mu = 35.87$ ). The redshift is derived from narrow emission lines visible in the transient spectra ( $\text{H}\alpha$  and  $[\text{O III}] 5007 \text{ \AA}$ ). The optical spectrum of the host galaxy taken after the transient had faded below the detection threshold also confirmed this redshift (Appendix B). Galactic reddening in the direction of CSS 161010 is  $E(B - V) = 0.084$  mag (E. F. Schlafly & D. P. Finkbeiner 2011). Based on the absence of  $\text{Na I D}$  absorption lines in the transient spectra and the low luminosity of the host galaxy, we assume that the host galaxy extinction toward CSS 161010 is negligible. Using PROSPECTOR (B. D. Johnson et al. 2021), we find that the host’s spectra and photometry are consistent with a stellar mass of  $\log(M_*/M_\odot) = 8.135_{-0.079}^{+0.087}$  (details are discussed in Appendix B), higher than previously estimated by C20. This is mostly due to the  $z$ -band photometry that further constrains the stellar mass. By extrapolating the BH mass–stellar mass correlations (J. E. Greene et al. 2020), the stellar mass of the host galaxy suggests the existence of a possible BH with a mass of  $10^{2.9} - 10^{4.8} M_\odot$  (Figure 1), corresponding to an IMBH ( $10^2 M_\odot < M_{\text{BH}} < 10^5 M_\odot$ ; J. E. Greene et al. 2020). While the scaling relations are firmly established for supermassive BHs, they remain poorly constrained for IMBHs, and additional observations at lower BH masses are needed to check the validity of these relations. However, IMBH mass estimates in dwarf galaxies tend to follow the extrapolation of the scaling relations into the low-mass regime (e.g., A. E. Reines & M. Volonteri 2015; J. E. Greene et al. 2020) but with a larger scatter.

#### 3.2. Light Curves and Colors

In Figure 2, we present the light curves of CSS 161010. During the first 6 days after the start of the outburst, we obtained ASAS-SN  $V$ -band photometry, which allowed us to estimate a rise time of  $\sim 3.8$  days and a peak absolute  $V$ -band magnitude of  $M_V^{\text{max}} = -20.66 \pm 0.07$  mag. In 6.3 days from the start of the outburst (2.5 days from the maximum), CSS 161010 declines to half its peak flux. After the peak, it follows a power-law decline of  $\propto t^{-2.8 \pm 0.1}$  at all optical bands. Overall, the transient shows an extremely fast evolution and blue colors. These properties resemble those found in well-observed LFBOTs like AT 2018cow (S. J. Prentice et al. 2018; D. A. Perley et al. 2019), AT 2020mrf (Y. Yao et al. 2022),

and AT 2020xnd (D. A. Perley et al. 2021; A. Y. Q. Ho et al. 2022).

The intrinsic color curves of CSS 161010 are presented in the bottom panel of Figure 2. Color information is only available from  $\sim 9.4$  days postoutburst. At this point, CSS 161010 shows blue colors ( $g - r = -0.24$  mag,  $r - i = -0.38$  mag), which last for  $\sim 12$ – $15$  more days. From day 25 onward, the  $g - r$  and  $r - i$  colors become bluer, while  $i - z$  becomes redder, going from 0.14 mag at 23.8 days to 0.97 mag at 31.6 days. After this epoch,  $g - r$  also becomes redder. During the full period of observations, the  $r - i$  color remains blue, with a quasi-constant evolution at a mean value of  $\approx -0.24$  mag. From the imaging polarimetry obtained  $\sim 53$  days from the start of the outburst, we found that CSS 161010 shows a similar level of polarization as the surrounding field stars (5%–10% linear polarization). We therefore find that CSS 161010 does not show significant polarization above this level.

We constructed the bolometric light curve and estimated the blackbody temperatures and radii for CSS 161010 employing the SUPERBOL code (M. Nicholl 2018). We used the extinction-corrected  $BgVriz$  photometry. To have similar coverage in different bands at each epoch, we either interpolated or extrapolated the light curves using a low-order polynomial or obtained the magnitude from the nearest epochs using the  $V$  band as a reference filter and assuming a constant color. We then converted all magnitudes into fluxes at the effective wavelength of each filter and integrated them over the spectral energy distribution (SED). The flux outside the observed passbands was estimated by extrapolating the blackbody fit over all wavelengths.

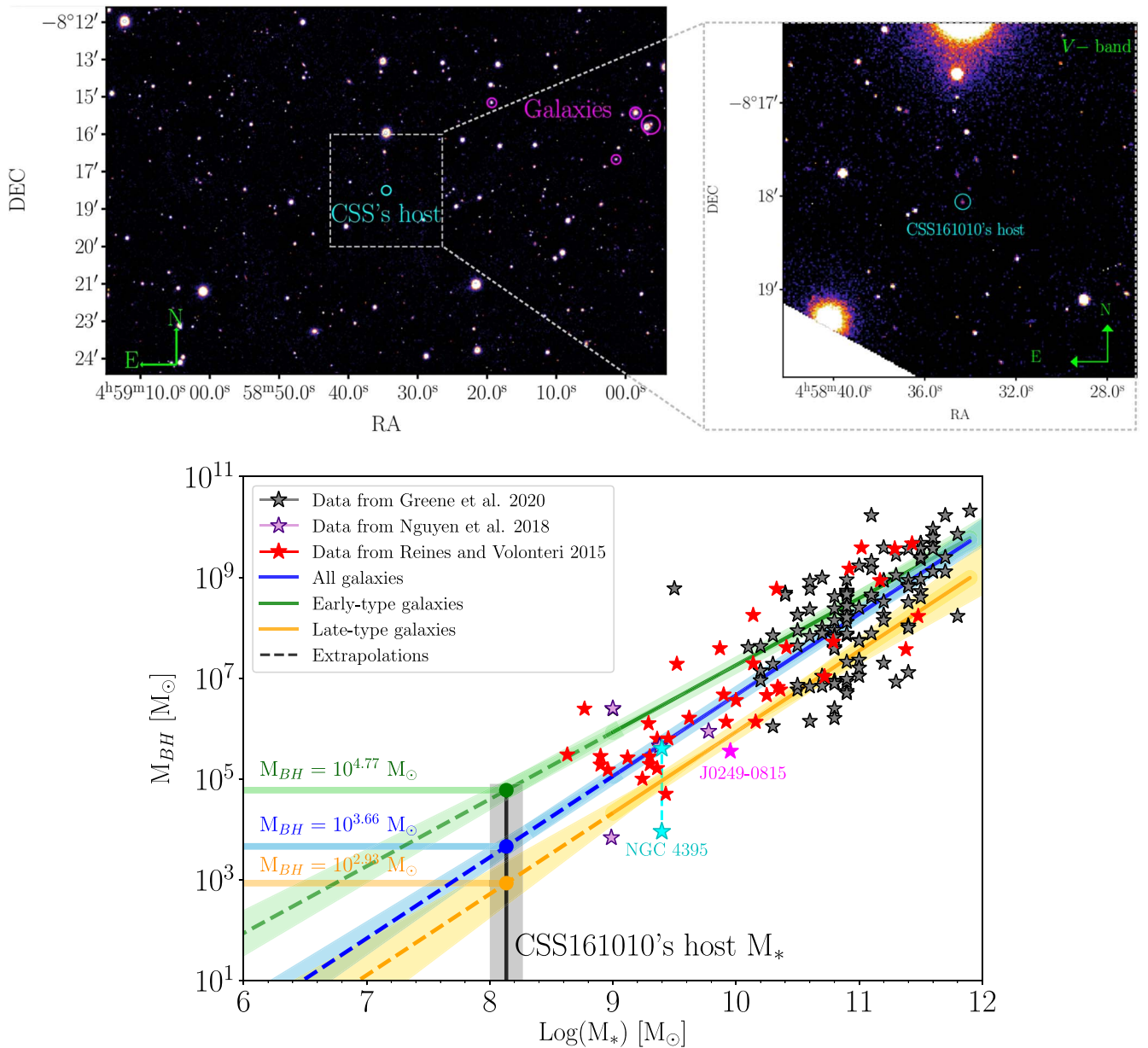
We found that CSS 161010 reached a peak luminosity of  $L_{\text{bol}} = (1.30 \pm 0.56) \times 10^{44} \text{ erg s}^{-1}$   $\sim 3.8$  days from the start of the outburst. After the peak, the bolometric light curve followed a power-law decline similar to that measured in the optical bands. Integrating over the observed epochs, we find a total radiated energy of  $(6.62 \pm 0.02) \times 10^{49} \text{ erg}$ . From  $\sim 2$  to 60 days, the blackbody temperature ( $T_{\text{BB}}$ ) shows roughly constant evolution at around  $T_{\text{BB}} \approx 15,000$ – $16,000$  K, while the blackbody radius ( $R_{\text{BB}}$ ) mimics the light-curve evolution: a fast rise to the peak, followed by a fast decline. It rises from  $R_{\text{BB}} = 1.1 \times 10^{15} \text{ cm}$  at  $\sim 2$  days to  $R_{\text{BB}} = 1.9 \times 10^{15} \text{ cm}$  at the peak. After that, the radius declines continuously until it reaches a value of  $R_{\text{BB}} = 3.7 \times 10^{13} \text{ cm}$  at  $\sim 61$  days (see Section 3.4).

#### 3.3. Spectroscopic Evolution

Figure 3 presents the optical spectroscopic evolution of CSS 161010 from 9.4 to 57.7 days from the start of the outburst. The spectra show a remarkable transformation from a blue and featureless continuum to spectra dominated by very broad, blueshifted emission lines with peculiar shapes and extremely high velocities.

The first spectrum, at 9.4 days, is characterized by a featureless blue continuum with a blackbody temperature of around  $T_{\text{BB}} \approx 16,000$ – $17,000$  K. One day later (10.4 days), the blackbody temperature decreased by  $\sim 500$  K, and the spectrum started to show some features between 4000 and 5000 Å. After a detailed inspection, we found that these can be explained by He II  $\lambda 4686$  and  $\lambda 5411$  emission lines at a velocity of  $\sim -33,000 \text{ km s}^{-1}$  (top panel of Figure 4). These lines are also visible at 11.3 days, but they are no longer detectable at 21.0 days. From 21.0 days onward, the spectra changed





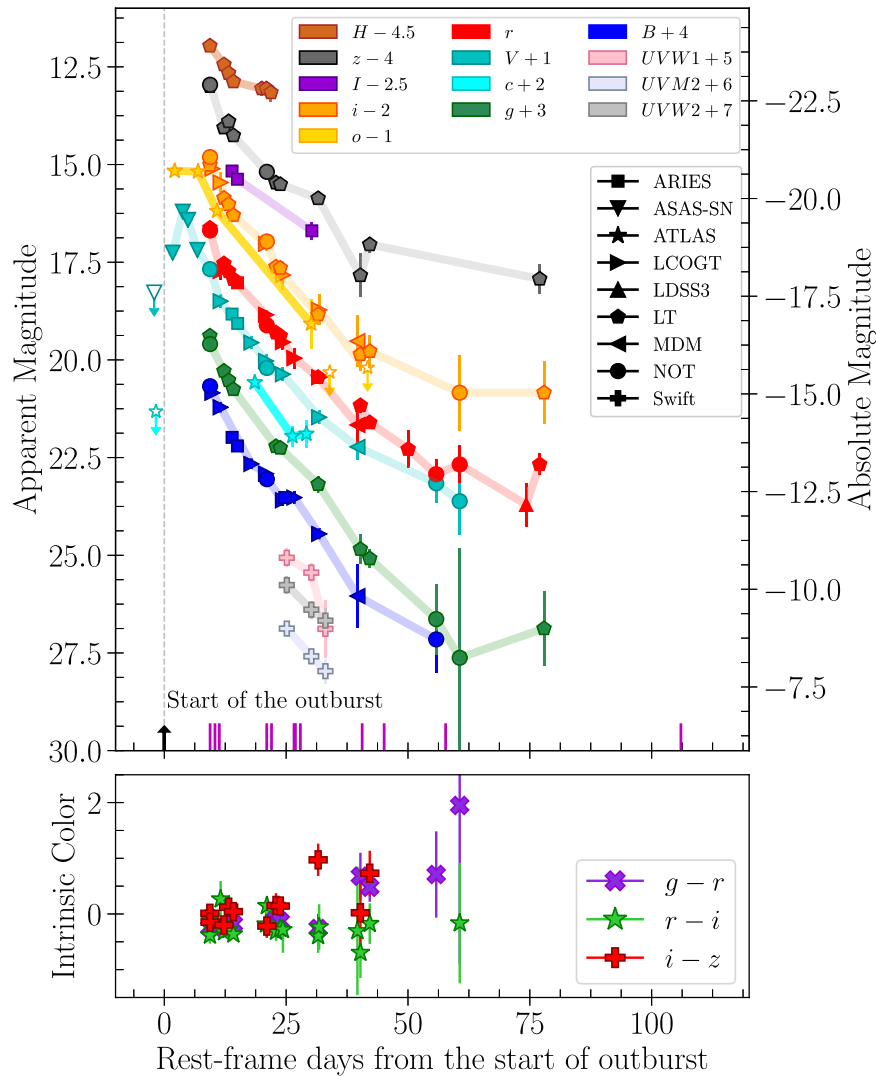
**Figure 1.** Top left: PS1 red, green, and blue false-color *gri* image of CSS 161010's field. The gray square is a zoom-in on the field around CSS 161010. Known galaxies in the field are marked with magenta circles. Top right: false-color IMACS/Magellan *V*-band image of the field around CSS 161010. The transient is located close to the center of its faint host. Bottom: relationship between BH mass ( $M_{BH}$ ) and stellar mass ( $M_{*}$ ) for a sample of galaxies (A. E. Reines & M. Volonteri 2015; D. D. Nguyen et al. 2018; J. E. Greene et al. 2020), NGC 4395 (lower value, M. den Brok et al. 2015; higher value, J.-H. Woo et al. 2019), and J0249–0815 (W. Zuo et al. 2024). The linear fits obtained by J. E. Greene et al. (2020) for the early-type (green), late-type (orange), and all galaxies (blue) are shown with solid lines. The extrapolations of these fits are shown with dashed lines. The estimated  $M_{*}$  of CSS 161010's host is indicated with a vertical black line, and the points where the fits cross it are highlighted with circles.

completely, and two broad emission features at  $\sim 4500\text{--}5000 \text{ \AA}$  and  $\sim 6000\text{--}6500 \text{ \AA}$  are now visible. These lines show an extraordinary evolution over time: they lack any absorption component, and their emission components evolve from a broad feature into a more complex, flat-topped profile with a blue shoulder (at  $\sim 26\text{--}28$  days) and finally, after 40 days, into a feature with a narrower asymmetric shape. We identify these two broad emission features as  $H\alpha$  and  $H\beta$  with blueshifted velocities between  $10,000 \text{ km s}^{-1}$  at  $\sim 21$  days and  $4000 \text{ km s}^{-1}$  at  $\sim 58$  days (offset velocities from the rest wavelength at the broad line profile maxima). To verify this identification, we compare their profiles and evolution. Figure 5 shows this

comparison from 21 to 45 days. Although the lower signal-to-noise in the blue part of the spectra prevents a detailed analysis of  $H\beta$ , we find that both profiles evolve consistently, confirming our initial identification of these lines. We found that the Balmer decrement is  $\sim 3$  until 28 days and perhaps a little smaller at later epochs.

The highest velocities of  $H\alpha$  and  $H\beta$  (the bluest parts of the profile) decrease from  $\sim -33,000 \text{ km s}^{-1}$  at 21.0 days to  $\sim -10,000 \text{ km s}^{-1}$  at 57.7 days (Appendix C, Figure C1), while the line center always remains blueshifted by more than  $4000 \text{ km s}^{-1}$ . The decreasing emission at the highest velocities is not unexpected, since it reflects the disappearance of the





**Figure 2.** Light and color curves of CSS 161010. Top: UV and optical light curves of CSS 161010. Upper limits are presented as open symbols. The start of the outburst is indicated by a vertical black arrow. The vertical magenta lines are the epochs of optical spectroscopy. The photometry is host-subtracted (except in the  $I$  band) and corrected for Milky Way extinction. Bottom: intrinsic color curves of CSS 161010.

fastest-moving material; however, the persistent blueshifted emission and the lack of any emission at the rest wavelength (or redshifted from it) are striking. To our knowledge, this type of evolution has never been seen in any other transient.

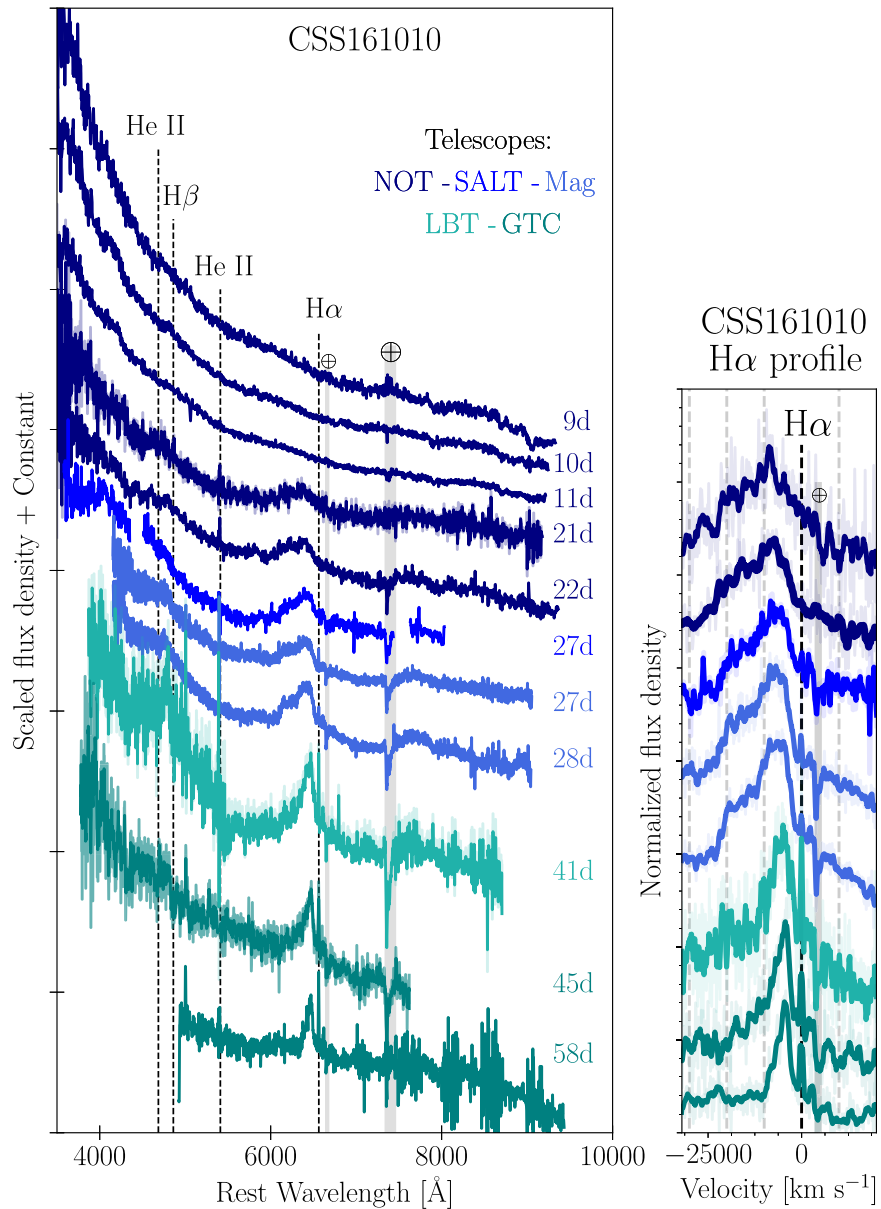
### 3.4. Comparison to Other LFBOTs

The fast photometric evolution of CSS 161010 is reminiscent of other LFBOTs. Here, we compare our photometric and spectroscopic observations with those available for LFBOT objects. The best-observed cases are AT2018cow, AT2020mrf, and AT2020xnd. Information on these objects is presented in Table F1 in Appendix F. In Figure 6, we show the  $g$ - and  $r$ -band light curves, bolometric light curve,  $g-r$  colors, blackbody temperature, and blackbody radius of CSS 161010 together with those of LFBOTs. From the light curves, we can see that CSS 161010 and AT2020mrf have almost identical rise times of 3.8 and 3.7 days, respectively, whereas AT2018cow has the fastest rise time of only 2.5 days. The rise time of AT2020xnd is uncertain due to the poor constraints on its prepeak light curve (D. A. Perley et al. 2021). However, it seems to rise between 2 and 5 days. At peak, the

brightest object is AT2020xnd ( $M_{5000}^{\max} \simeq -20.9 \pm 0.3$  mag), followed by AT2018cow ( $M_{4800}^{\max} \simeq -20.8 \pm 0.2$  mag), CSS 161010 ( $M_{5500}^{\max} = -20.7 \pm 0.1$  mag), and AT2020mrf ( $M_{4200}^{\max} \simeq -20.0 \pm 0.2$  mag).<sup>46</sup> After the peak, they have similar decline rates and share similar blue  $g-r$  colors up to  $\sim 30$  days postoutburst, when a deviation toward redder colors is observed in CSS 161010.

Figure 7 shows the spectra of CSS 161010 at three different phases compared with these LFBOTs (left panels). Before 10 days after the start of the outburst, all spectra are characterized by a featureless blue continuum. After this phase, where we only have spectroscopic data for AT2018cow and CSS 161010, considerable differences appear. After  $\sim 20$  days, the spectrum of CSS 161010 shows broad blueshifted hydrogen emission profiles, while He I lines dominate the spectrum of AT2018cow. Later, at  $\sim 45$  days, the emission lines of both CSS 161010 and AT2018cow become narrower, more significantly so in the former.

<sup>46</sup> CSS 161010 and AT2020mrf were only observed in one band around the peak.



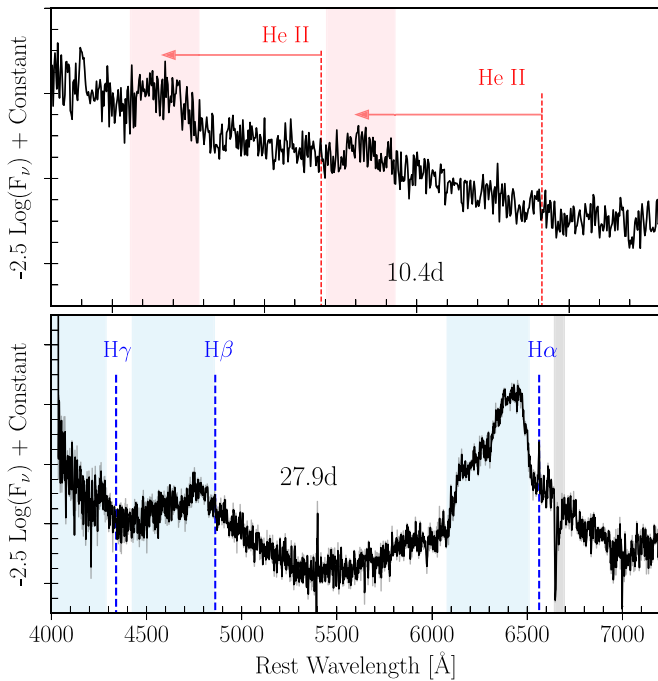
**Figure 3.** Spectral sequence of CSS 161010 from 9.4 to 57.7 days from the start of the outburst ( $JD = 2457669.92 \pm 2.00$ ). The phases are labeled on the right. Each spectrum has been corrected for Milky Way extinction and shifted vertically for presentation. A zoom-in around the  $H\alpha$  P Cygni profile in velocity space from 21 to 58 days is shown in the smaller right panel. Note the blueshift of  $H\alpha$  at all epochs.

### 3.5. Comparison to Hydrogen-rich SNe and TDEs

One of the main characteristics of CSS 161010 is the presence of hydrogen lines in its spectra. Based on this property, we compare CSS 161010’s light curves and spectra with hydrogen-rich SNe (SNe II) and TDE candidates in Figures 6 and 7. We selected well-studied objects of each of these classes; these are SN 1979C (a fast-declining SN II with a shallow  $H\alpha$  absorption feature; N. Panagia et al. 1980), SN 2008es (SLSN II; S. Gezari et al. 2009), and three hydrogen-rich TDE candidates: AT 2018zr (T. W. S. Holoiien et al. 2019; P. Charalampopoulos et al. 2022), AT 2020neh (C. R. Angus et al. 2022), and AT 2020wey (P. Charalampopoulos et al. 2023). Details of the comparison sample are presented in Table F1. From their photometric properties (Figure 6), we see that CSS 161010 differs entirely from these hydrogen-rich events. The photometric evolution of hydrogen-rich SNe and TDE candidates is much slower, and their

intrinsic colors are redder than those of CSS 161010. They also have lower  $T_{BB}$  (except for AT 2020wey; Figure 6) and larger  $R_{BB}$ . Spectroscopically (Figure 3), all objects are characterized by a featureless blue continuum in the early phases, but they begin to differ as the lines appear. Although SN 1979C and CSS 161010 both show  $H\alpha$ , their profiles are dissimilar. The  $H\alpha$  profile of SN 1979C is bell-shaped, with a slightly blueshifted peak emission ( $< -2000 \text{ km s}^{-1}$ ). Blueshifted emission line peaks evolving to become rest-frame-centered is a known property in SNe (L. Dessart & D. J. Hillier 2005; J. P. Anderson et al. 2014). In the case of the SLSN II SN 2008es, the  $H\alpha$  appears later (after  $\sim 100$  days; S. Gezari et al. 2009) and, during the comparison phases, shows different spectroscopic properties from CSS 161010.

When comparing CSS 161010 with TDE candidates, we see a large diversity. Unlike CSS 161010, AT 2018zr and AT 2020neh have an  $H\alpha$  profile centered at the rest



**Figure 4.** Lines identified in the spectra of CSS 161010 at  $\sim 10.4$  and  $\sim 27.9$  days after the start of the outburst. The dashed lines indicate the rest position of the helium (top) and hydrogen (bottom) lines. The shaded regions mark their blueshifted locations.

wavelength; AT 2018zr has a symmetric line profile, but AT 2020neh does not. Both objects lack absorption features. For AT 2020neh, blueshifted lines were detected at late phases ( $\sim 212$  days from the start of the outburst) and linked to optically thick outflowing material (C. R. Angus et al. 2022). Similar blueshifted profiles at very late times have been observed in SNe II and attributed to dust formation (e.g., SN 1998S, SN 2007od; D. C. Leonard et al. 2000; J. E. Andrews et al. 2010). Regardless of this, their line profiles are different from CSS 161010. The spectral comparison with AT 2020wey is more interesting. At around 28–31 days, the spectra of CSS 161010 and AT 2020wey appear similar. In particular, their  $H\alpha$  profiles are almost identical. The only difference is the missing redder part of the line profiles of CSS 161010 (i.e., the entire profiles are blueshifted). However, later, at 45–48 days, these two objects show very different spectra. TDEs often show blueshifted hydrogen line profiles with peculiar shapes (N. Roth & D. Kasen 2018). This property is also observed in CSS 161010, and from all the objects included in the comparison sample, the hydrogen-rich TDE AT 2020wey is the most similar, although it has a distinctly slower luminosity evolution and a much larger  $R_{\text{BB}}$  after  $\sim 10$  days.

### 3.6. Discussion

Some well-studied LFBOTs were found in dwarf star-forming galaxies (e.g., D. L. Coppejans et al. 2020; A. Y. Q. Ho et al. 2020; Y. Yao et al. 2022) and thus have been considered likely to be associated with massive stars. We found that CSS 161010’s host has very similar properties to AT 2020xnd’s host: both have a small stellar mass ( $\log(M_*/M_\odot) = 8.13$  and 8.48) and a modest star formation rate ( $\text{SFR}(M_\odot \text{ yr}^{-1}) = 0.015$  and 0.020, respectively). Recently, two LFBOTs were found in more massive galaxies. A. Y. Q. Ho et al. (2023a) found that

AT 2022tsd was located  $\sim 6$  kpc from the center of a star-forming galaxy ( $\log(M_*/M_\odot) = 9.96$ ), while A. A. Chrimes et al. (2024a, 2024b) found that AT 2023fhn is 16.5 kpc from the center of the nearest spiral galaxy and 5.4 kpc from an apparent dwarf companion ( $\log(M_*/M_\odot) = 9.97$  considering the spiral and satellite galaxies together), both objects representing a deviation in terms of their environments from previous LFBOTs. Both A. Y. Q. Ho et al. (2023a) and A. A. Chrimes et al. (2024a) favored a core-collapse event to explain these transients, although they did not rule out the IMBH TDE interpretation.

#### 3.6.1. Stellar Explosion Scenario

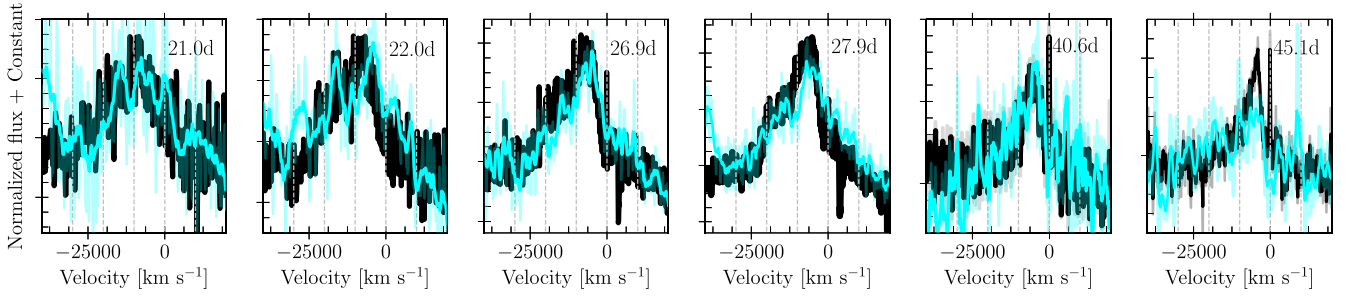
C20 found that CSS 161010’s X-ray and radio observations alone can be explained equally well by a stellar explosion or a TDE. Based on our optical observations, we find a stellar explosion to be unlikely. The presence of entirely blueshifted emission line profiles throughout the evolution is challenging to explain in any SN scenario. The  $R_{\text{BB}}$  evolution is also inconsistent with the homologous expansion expected in any SN (L.-D. Liu et al. 2018). Furthermore, the radioactively powered SN mechanism is unrealistic. Assuming that CSS 161010 arises from a stellar explosion where all the energy is from radioactive decay, we can estimate the ejecta mass and the amount of  $^{56}\text{Ni}$  synthesized during the explosion by fitting the Arnett model (W. D. Arnett 1982). Thus, considering a rise time (3.8 days), a canonical SN kinetic energy ( $\sim 10^{51}$  erg), an opacity of  $\sim 0.1 \text{ cm}^{-2} \text{ g}^{-1}$ , and  $\beta = 13.7$  (see S. J. Prentice et al. 2016), we derive an ejecta mass,  $M_{\text{ej}} \sim 0.3 M_\odot$ . Since  $^{56}\text{Ni}$  powers the main peak, and using the rise time and the peak luminosity of the bolometric light curve, we estimate a  $^{56}\text{Ni}$  mass of  $M_{\text{Ni}} = 2.2 M_\odot$ . The small  $M_{\text{ej}}$  explains the fast rise, while the large amount of  $^{56}\text{Ni}$  explains the peak luminosity. Given that  $M_{\text{Ni}}$  is much larger than  $M_{\text{ej}}$ , this scenario would be unphysical. Additionally, considering that the spectra show prominent hydrogen lines, the  $M_{\text{ej}}$  must also contain some hydrogen, making this inconsistency even greater.

Recent studies (e.g., O. D. Fox & N. Smith 2019; D. Xiang et al. 2021; C. Pellegrino et al. 2022) have found similarities between LFBOTs and Type Ibn SNe and suggest that these fast-evolving objects can be explained by the ejecta interacting with helium-rich circumstellar material (CSM). D. Xiang et al. (2021) found that the bolometric light curve of AT 2018cow can be fitted by a hybrid model that includes  $^{56}\text{Ni}$  and the interaction of the SN ejecta with a dense CSM. The spectra of AT 2018cow were argued to support this alternative scenario because they are dominated by narrow helium emission lines (O. D. Fox & N. Smith 2019; C. Pellegrino et al. 2022). AT 2018cow and CSS 161010 have similar light curves (Figure 6), so we might expect CSS 161010 to also have a comparable powering mechanism ( $^{56}\text{Ni}$  plus CSM). However, unlike AT 2018cow, the spectra of CSS 161010 are dominated by very broad and entirely blueshifted hydrogen features. In CSS 161010, we only detect narrow lines at late phases, and those lines are associated with the host galaxy. Therefore, the spectral properties of CSS 161010 do not support these scenarios.

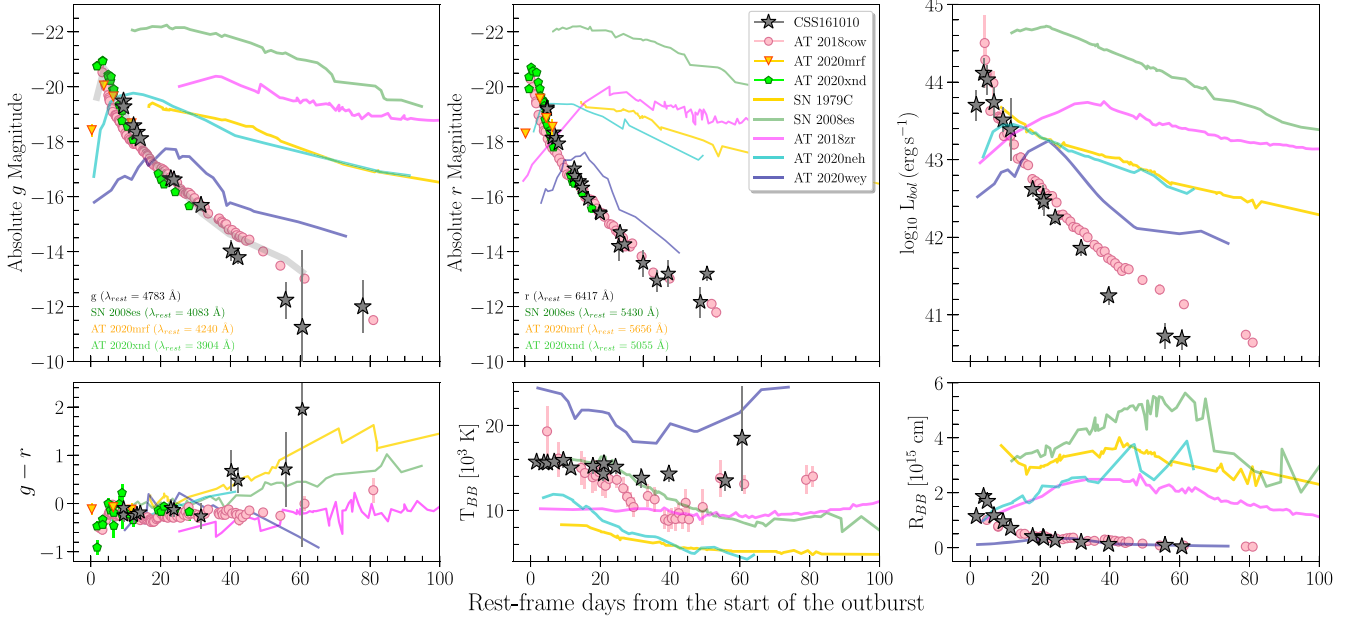
#### 3.6.2. Wolf–Rayet/BH Mergers

The Wolf–Rayet star/BH (or neutron star) merger scenario recently proposed for AT 2018cow (B. D. Metzger 2022) seems problematic for CSS 161010 because of the strong





**Figure 5.** Comparison of the H $\alpha$  (black) and H $\beta$  (cyan) profiles from 21.0 to 57.7 days from the start of the outburst. The phases are labeled on the top of each panel. The vertical dashed lines mark the velocities at  $-30,000$ ,  $-20,000$ ,  $-10,000$ ,  $0$ , and  $10,000$  km s $^{-1}$ . To match both profiles, we multiplied H $\beta$  by 3 in the first four panels and by 2 in the last two.



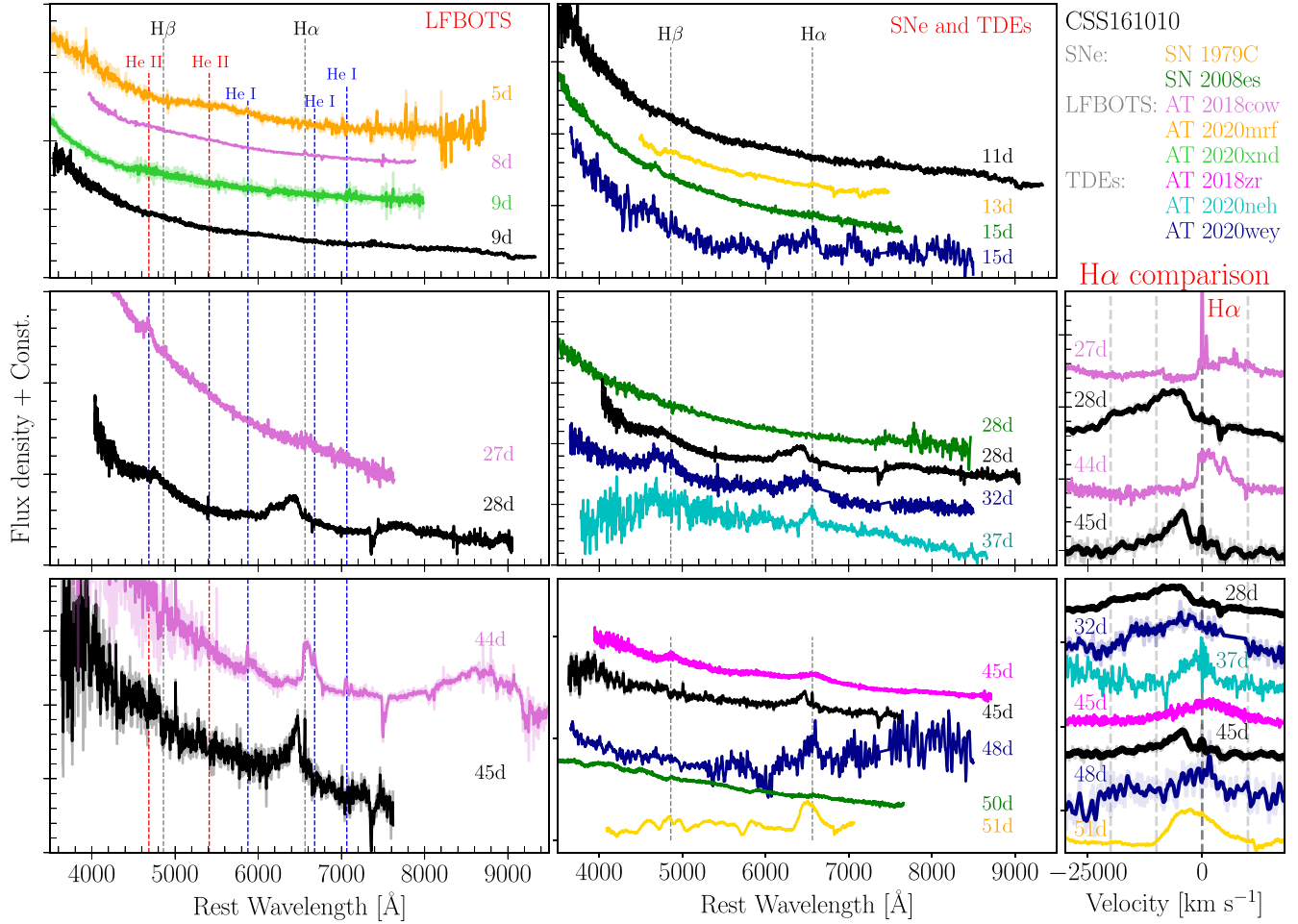
**Figure 6.** Top panels: CSS 161010  $g$ -band (left),  $r$ -band (middle), and bolometric light curves (right) compared with the well-sampled LFBOT AT 2018scw (purple circles); SNe with hydrogen in their spectra: SN 1979C (SN II), SN 2008es (superluminous SN II); and three hydrogen-rich TDE candidates: AT 2018zr, AT 2020neh, and AT 2020wey. In the  $g$ - and  $r$ -band light-curve comparisons, the LFBOTs with good optical coverage, AT 2020mrf (yellow downward-facing triangles) and AT 2020xnd (green pentagons), are also included. The CSS 161010  $V$ -band light curve is also shown (thick gray line; left panel). Details of the comparison sample are presented in Table F1. Bottom panels:  $g - r$  colors (left), blackbody temperature (middle), and blackbody radius (right) of CSS 161010 compared with SN 1979C, SN 2008es, AT 2018scw, AT 2018zr, AT 2020neh, and AT 2020wey. JD = 2457669.92  $\pm$  2.00 is the start of the outburst estimated for CSS 161010.

blueshifted hydrogen lines. While the scenario allows the presence of hydrogen in a pre-SN disklike structure, the orbital velocity of this disk is at least an order of magnitude slower than the observed  $c/10$ . Acceleration by an outflow from the central engine would be needed, combined with rapid cooling of the shocked gas to allow for efficient Balmer line emission. The situation could be similar to that of a cool, dense shell in SNe interacting with a dense surrounding medium (e.g., R. A. Chevalier & C. Fransson 1994). The shocked disk would have a density of  $\gtrsim 10^9 (T/10^8 \text{ K})^{0.5} \text{ cm}^{-3}$  ( $T$  is the temperature of the shocked gas) to have a cooling time of  $\lesssim 10$  days (e.g., C. Fransson et al. 1996). The gas cools under compression so that H $\alpha$ -emitting gas would be orders of magnitude denser. Under these circumstances, Balmer decrements of  $\sim 10$  are not unusual (e.g., F. Taddia et al. 2020), in contrast to the Case B ratio of  $\sim 3$  we observe. It is also unclear why the merger scenario should result in strong blueshifts.

The Case B H $\alpha$  emission per cm $^{-3}$  is  $\varepsilon_{\text{H}\alpha} = 3.51 \times 10^{-25} T_4^{0.96} n_e n_p f^2$  (D. E. Osterbrock & G. J. Ferland 2006), and if  $V_{\text{em}}$  is the volume of the gas emitting H $\alpha$ , then the H $\alpha$

luminosity is  $L_{\text{H}\alpha} = \varepsilon_{\text{H}\alpha} V_{\text{em}}$ . Here  $T_4$  is the gas temperature in  $10^4$  K,  $f$  is the filling factor of the emitting gas, and  $n_e$  and  $n_p$  are the electron and proton number densities, respectively. For a helium-to-hydrogen number density ratio of 0.1 and fully ionized hydrogen, the mass of this volume is  $M_{\text{em}} = 1.4 m_p n_p V_{\text{em}}$ , or  $M_{\text{em}} = 0.33 T_4^{0.96} (f n_{e,8})^{-1} L_{\text{H}\alpha,40} M_{\odot}$ , where  $n_{e,8}$  is in units of  $10^8 \text{ cm}^{-3}$  and  $L_{\text{H}\alpha,40}$  in  $10^{40} \text{ erg s}^{-1}$ . For an ejected mass of  $0.1 M_{\odot}$  and a temperature of  $10^4$  K, this means that  $n_{e,8} \gtrsim 3.3 L_{\text{H}\alpha,40}$ . We measured  $L_{\text{H}\alpha,40} \approx 0.3$  when H $\alpha$  was first detected on day 21 and peaking at  $L_{\text{H}\alpha,40} \approx 1.7$  one week later, translating into  $n_{e,8} \gtrsim 0.95$  and  $\gtrsim 5.6$ , respectively.

The Case B recombination time of hydrogen is  $(\alpha_B n_e)^{-1}$ , where  $\alpha_B = 2.59 \times 10^{-13} T_4^{0.86} \text{ cm}^{-3} \text{ s}^{-1}$  (D. E. Osterbrock & G. J. Ferland 2006) and is less than 1 day for  $n_{e,8} \gtrsim 0.45 T_4^{0.86}$ . This implies a steady state between ionization and recombination, potentially with a time lag. If  $\dot{N}_{\text{ion},50}$  is the number of ionizing photons per second in units of  $10^{50} \text{ s}^{-1}$  put out by the central source, and  $\Omega/4\pi$  is the solid angle subtended by the H $\alpha$ -emitting region as seen by the central source,



**Figure 7.** Left panels: spectral comparison of CSS 161010 with the AT 2018cow-like objects: AT 2018cow, AT 2020xnd, and AT 2020mrf at different epochs. Middle panels: spectral comparison of CSS 161010 with fast-declining hydrogen-rich events: SNe 1979C and 2008es and the TDE candidates AT 2018zr, AT 2020neh, and AT 2020wey. Each spectrum has been shifted in flux for comparison. The vertical dashed lines indicate the rest wavelength positions of a selection of spectral lines. Right panels: CSS 161010 H $\alpha$  profile in velocity space compared with AT 2018cow (top) and the fast-declining hydrogen-rich SN 1979C and the TDE candidates AT 2018zr, AT 2020neh, and AT 2020wey (bottom). Vertical dashed lines in the middle and right panels mark the velocities at  $-20,000$ ,  $-10,000$ ,  $0$ , and  $10,000$  km s $^{-1}$ .

$\dot{N}_{\text{ion},50} \approx 74(\Omega/4\pi)^{-1}T_4^{0.1}L_{\text{H}\alpha,40}$ . Here we have assumed that the total Case B recombination rate in the H $\alpha$ -emitting region is  $\alpha_B n_e n_p f^2 V_{\text{em}}$ . If we use  $L_{\text{H}\alpha,40}$  from 21 and 28 days, then the corresponding values for  $(\Omega/4\pi)\dot{N}_{\text{ion},50}$  are  $\approx 21$  and  $\approx 120$ , respectively. This is in stark contrast to what is expected from blackbody spectra with the properties in Figure 6. At 21 (28) days, blackbodies only generate  $\dot{N}_{\text{ion},50} \sim 15$  (3.6). A possible solution is that there is a  $\sim$ three-week delay between the emitted ionizing radiation and H $\alpha$  emission due to geometry and light travel time, so that the number of ionizing photons reaching the H $\alpha$  cloud on day 28 may correspond to an epoch close to the peak of the bolometric luminosity in Figure 6. The luminosity is then some  $\sim 35$  times higher than on day 28 and  $\dot{N}_{\text{ion}} \sim 40$  times larger (for a blackbody spectrum). A three-week geometric delay between continuum and H $\alpha$  emission would mean that the distance between the H $\alpha$ -emitting regions and the central source is  $\gtrsim 8 \times 10^{16}$  cm. Similar arguments for light travel time effects in TDEs are discussed by P. Charalampopoulos et al. (2022). A problem with this interpretation is that  $(\Omega/4\pi)$  is expected to be much less than unity for such a distance and that we see He II lines much earlier than H $\alpha$ .

It is, therefore, likely that a pure blackbody spectrum from a central source cannot produce enough ionizing radiation. One

obvious candidate for the “extra” ionizing radiation is the X-ray emission observed by C20, which for their assumed spectrum with energy distribution  $\propto \nu^{-1}$  had a luminosity of  $\sim 4 \times 10^{39}$  erg s $^{-1}$  between 0.3 and 10 keV three to four months after optical peak. Extrapolating to lower energies, this would mean a rate of the number of ionizing photons from the X-ray source that is  $N_{\text{ion},X,50} \sim 0.5$ . If the process is similar to that in active galactic nuclei (AGN; i.e., inverse Compton scattering), the number of ionizing photons from the X-ray source is roughly proportional to the optical/UV luminosity. This could mean  $N_{\text{ion},X,50} \gtrsim 100$  close to the optical peak, which would still only account for  $\sim 10^{-3}$  of the total number of blackbody photons. Interestingly, the X-ray properties for AT 2018cow derived by R. Margutti et al. (2019) indicate that it had  $N_{\text{ion},X,50} \sim 300$  around 10 days. The upper limit from the stacked Swift X-Ray Telescope (XRT) data for CSS 161010 at 29.5 days (see Appendix A.1) corresponds to  $N_{\text{ion},X,50} \leq 31$ , assuming a flux distribution that is  $\propto \nu^{-1}$ . With the evolution of AT 2018cow as a template, this would mean  $N_{\text{ion},X,50} \lesssim 70$  (200) at 10 days (and at peak) for CSS 161010. There is thus room for sufficient X-ray emission to ionize the line-emitting gas.

A picture emerges where the fastest line-emitting gas expands with a speed of  $\sim c/10$  and is, like in AGN, ionized mainly by the X-ray emission. After 11 (28) days, when weak He II lines are first seen (and when  $H\alpha$  is the strongest), this gas has reached  $\sim 3$  (7)  $\times 10^{15}$  cm. Light travel time can only account for a few days of delay if the ionizing source is central. We find it more likely that the X-rays are produced over a larger volume, possibly in a jetlike structure as expected in TDEs (see, e.g., P. Charalampopoulos et al. 2022). The extent of the X-ray-emitting region can be estimated from the expansion of the mildly relativistic blast wave in the models of C20 for the same epochs, which are  $\sim 2$  (4.5)  $\times 10^{16}$  cm. This picture seems incompatible with the Wolf–Rayet star/compact object merger scenario. However, it is consistent with a TDE where time lags between the broadband light curves and the fluxes of broad emission lines have been observed, with shorter lags for, e.g., He I than  $H\alpha$  (see, e.g., P. Charalampopoulos et al. 2022; S. Faris et al. 2024).

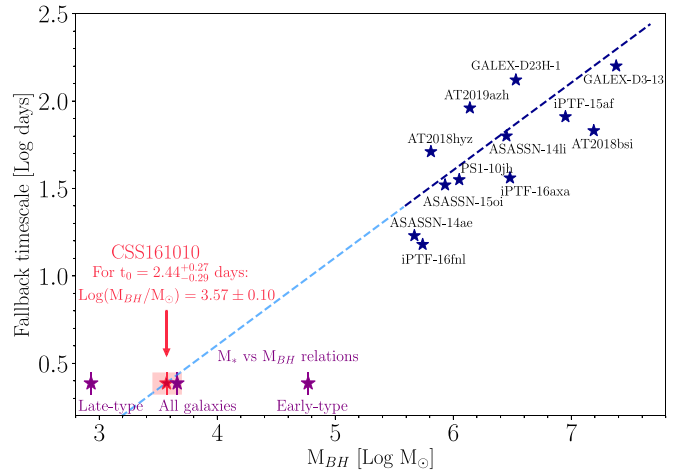
### 3.6.3. TDE from an IMBH Scenario

For a number of reasons, we find that a TDE appears to be the least problematic explanation for the spectroscopic and photometric properties of CSS 161010 and also fits with the arguments about  $H\alpha$  and light travel times above.

The entirely blueshifted line profiles of CSS 161010 at all epochs can be explained as a result of outflows occurring in TDEs as previously seen in X-rays (E. Kara et al. 2016) but also in blueshifted UV/optical emission/absorption lines (T. Hung et al. 2019; M. Nicholl et al. 2020). In fact, D. L. Coppejans et al. (2020) concluded that CSS 161010 has a mildly relativistic, decelerating outflow with an initial velocity of  $\Gamma\beta c > 0.55c$  that decreases to  $\sim c/3$  after 1 yr. Some TDEs are known to launch a relativistic jet, e.g., the well-observed case Swift J164449.3+573451 (D. N. Burrows et al. 2011). In the case of Arp 299-B AT1, interpreted as a TDE, very long baseline interferometry observations revealed an expanding and decelerating radio jet with an average intrinsic speed of  $0.22c$  (S. Mattila et al. 2018), which is quite similar to the outflow speed estimated for CSS 161010 at the late times.

Furthermore, the peak bolometric luminosity of CSS 161010,  $L_{\text{bol}} = 1.30 (\pm 0.56) \times 10^{44} \text{ erg s}^{-1}$ , implies a highly super-Eddington accretion phase (for a BH mass of  $10^{2.93} - 10^{4.77} M_{\odot}$ , the Eddington luminosity is  $L_{\text{Edd}} = (1-70) \times 10^{41} \text{ erg s}^{-1}$ ). Although very highly super-Eddington accretion can be expected in TDEs (A. Sądowski et al. 2016), the effect is not expected to be as large for the optical luminosities, making the lowest BH masses less likely. In any case, strong outflows are expected (N. I. Shakura & R. A. Sunyaev 1973; G. V. Lipunova 1999), and for a TDE produced by an IMBH, we expect these outflows to be much stronger and persist longer than for a supermassive BH because the super-Eddington mass fallback to the BH is predicted to persist for extended periods (S. Wu et al. 2018). Moreover, the lack of any absorption component in the optical lines can also be interpreted as a result of an outflow (N. Roth & D. Kasen 2018). The disappearance of the bluest part (highest velocity) of the  $H\alpha$  profile may also be explained as the result of an outflow that expands with time (N. Roth & D. Kasen 2018).

The continuous decay of  $R_{\text{BB}}$  after only  $\sim 3-4$  days from the start of the outburst can be described within the framework of TDEs (L.-D. Liu et al. 2018). Here, the  $R_{\text{BB}}$  of CSS 161010 is within the typical values found for TDEs (T. W. S. Holdeen et al. 2019; P. Charalampopoulos et al. 2022, 2023;



**Figure 8.** Correlation between the BH mass and TDE light-curve decay time (S. van Velzen et al. 2020). The dashed blue line shows the expected relation between  $t_{\text{fb}}$  and  $M_{\text{BH}}$  for a star of  $1 M_{\odot}$ . This line is extended (light blue) to lower values. The red star marks the location of CSS 161010 obtained by extending the  $t_{\text{fb}}$  and  $M_{\text{BH}}$  correlation. The red rectangle shows the uncertainty obtained from the light-curve fitting (Appendix D, Figure D1). Purple stars show the BH masses obtained from the  $M_{\odot}$  and  $M_{\text{BH}}$  relations (Figure 1; Appendix B). Reproduced and modified from S. van Velzen et al. (2020).

$\sim 10^{14}-10^{15}$  cm). Moreover, the fast light-curve decline rates could be explained as a partial TDE, in which a stellar remnant survives the interaction. Simulations have shown that the mass fallback rate to the BH in a partial TDE differs substantially from a  $t^{-5/3}$  power law expected for a total tidal disruption (M. J. Rees 1984) and decays with a steep power law of anywhere from  $t^{-2}$  to  $t^{-5}$  (E. R. Coughlin & C. J. Nixon 2019; T. Ryu et al. 2020). Hydrodynamic simulations (F. Kiroğlu et al. 2023) of a close encounter between a  $1 M_{\odot}$  main-sequence star and a  $10^2-10^4 M_{\odot}$  IMBH found that a small amount of material is stripped from the star at each pericenter passage with a period of a few  $\times 10^3$  yr for a  $10^4 M_{\odot}$  BH. The star is eventually fully disrupted or ejected. The simulations predict highly super-Eddington accretion rates and brief flares with peak luminosities between  $10^{44} \text{ erg s}^{-1}$  and  $3 \times 10^{44} \text{ erg s}^{-1}$  for BH masses in the range  $10^3-10^4 M_{\odot}$ . These predicted peak luminosities are similar to that observed for CSS 161010, providing additional support for this scenario.

The fallback timescale ( $t_{\text{fb}}$ ) measured from the TDE’s light curve can provide an independent BH mass estimate (N. Blagorodnova et al. 2017; S. van Velzen et al. 2020; A. Mummery et al. 2024). This fallback timescale has been estimated for a sample of TDEs by fitting a power-law decay ( $L_{\text{bb}} \propto (t/t_0)^p$ ) to their bolometric light curves with the power-law index fixed,  $p = -5/3$ . As the characteristic decay time ( $t_0$ ) is comparable to the theoretical  $t_{\text{fb}}$  (S. van Velzen et al. 2019), it is possible to derive the BH mass. Fitting the bolometric light curve of CSS 161010, we found  $t_0 = 2.44^{+0.27}_{-0.29}$  days (Appendix D1), which implies a BH mass of  $10^{3.57 \pm 0.10} M_{\odot}$  (Figure 8) consistent with our estimates based on the host galaxy’s stellar mass; this corroborates CSS 161010 as a TDE candidate with one of the lowest BH masses to date.

Most low-redshift IMBH candidates have been found in low-mass, star-forming dwarf galaxies (M. Mezcua et al. 2016) through kinematic studies or by extrapolating the scaling relations between the BH properties and galaxy parameters. Observations of AGN, gravitational-wave signals, and TDEs have provided further evidence for their existence



(D. Donato et al. 2014; M. Mezcua 2017; D. Lin et al. 2018; R. Abbott et al. 2020; J. E. Greene et al. 2020; J. S. He et al. 2021; S. Wen et al. 2021; C. R. Angus et al. 2022). Although an IMBH is not expected to exist in every dwarf galaxy, simulations (J. M. Bellovary et al. 2019) indicate that the BH occupation fraction rapidly increases in galaxies with stellar masses above  $10^8 M_{\odot}$ , with roughly 60% of  $10^{8.3} M_{\odot}$  galaxies hosting an IMBH. For CSS 161010, we measured an offset of  $0''.383 \pm 0''.024$  (a projected distance of  $\sim 300$  pc; Appendix E) from the host galaxy’s center. Although supermassive BHs are located at the centers of their host galaxies, IMBHs in dwarf galaxies are not all expected to coincide with the galaxy nucleus (D. Lin et al. 2018). In fact, recent simulations (J. M. Bellovary et al. 2019) indicate that half of the IMBHs in dwarf galaxies are more than 400 pc from the centers. BH growth in low-mass galaxies is expected to be stunted by SN feedback (M. Habouzit et al. 2017), so dwarf galaxies in the local Universe that have evolved in isolation can host BHs with masses comparable to the seed BHs in the early Universe.

#### 4. Summary

We presented photometric and spectroscopic observations of CSS 161010. We found that the light curves of CSS 161010 are characterized by an extremely fast evolution and blue colors. CSS 161010 reaches an absolute peak of  $M_V^{\max} = -20.66 \pm 0.06$  mag in 3.8 days from the start of the outburst. After maximum, CSS 161010 follows a power-law decline  $\propto t^{-2.8 \pm 0.1}$  at all optical bands. These photometric properties are comparable to those shown by well-observed LFBOTs. However, unlike these objects, the spectra of CSS 161010 are dominated by very broad blueshifted hydrogen emission lines starting at  $\sim 20$  days from the start of the outburst. Our analysis shows any stellar explosion scenario to be unlikely and that CSS 161010 is most naturally explained as a hydrogen-rich star (partially) disrupted by an IMBH. Multiwavelength observations of other LFBOTs (D. R. Pasham et al. 2021; W. Zhang et al. 2022; Y. Chen et al. 2023; A. Y. Q. Ho et al. 2023a; A. Inkenhaag et al. 2023) provide strong evidence favoring a central engine. Although the nature of the engine is unknown, a TDE by an IMBH is a plausible scenario in several cases (A. Y. Q. Ho et al. 2023a; A. Inkenhaag et al. 2023). In fact, we argue that from a spectroscopic point of view, CSS 161010 provides the most convincing case to date. If other LFBOTs, in addition to CSS 161010 and AT 2018cow, can be explained as a TDE by an IMBH, further observations of such events could be used for pinpointing otherwise quiescent IMBHs, constraining their masses, occupation fractions, host galaxy properties, and galactocentric distances.

#### Acknowledgments

We thank the anonymous referee for the comments and suggestions that helped us improve the paper. We thank Keiichi Maeda, Masaomi Tanaka, Hanindyo Kuncarayakti, Takashi Nagao, and Taeho Ryu for valuable discussions; Anna Ho and Daniel Perley for discussing the physical properties of LFBOTs during the *Interacting Supernovae* MIAPbP meeting; Sjoert Van Velzen for sharing the data to reproduce Figure 8; and Francesco Coti Zelati for helpful discussion about the X-ray observations and upper limits. We are grateful to Nidia Morrell for performing some of the observations used in this work.

C.P.G., S.M., and L.D. thank the Munich Institute for Astro-, Particle and BioPhysics (MIAPbP), which is funded by the Deutsche Forschungsgemeinschaft (DFG, German Research Foundation) under Germany’s Excellence Strategy—EXC-2094—390783311, for the useful discussions.

C.P.G. acknowledges financial support from the Secretary of Universities and Research (Government of Catalonia) and by the Horizon 2020 Research and Innovation Programme of the European Union under the Marie Skłodowska-Curie and the Beatriu de Pinós 2021 BP 00168 program, from the Spanish Ministerio de Ciencia e Innovación (MCIN) and the Agencia Estatal de Investigación (AEI) 10.13039/501100011033 under the PID2020-115253GA-I00 HOSTFLOWS project, and the program Unidad de Excelencia María de Maeztu CEX2020-001058-M. S.M. and T.M.R. acknowledge financial support from the Research Council of Finland project 350458. P.L. acknowledges support from the Swedish Research Council. S.G.G. acknowledges support by FCT under Project No. UIDB/00099/2020. P.G.J. has received funding from the European Research Council (ERC) under the European Union’s Horizon 2020 research and innovation program (grant agreement No. 101095973). S.D. acknowledges the National Natural Science Foundation of China (grant No. 12133005) and the New Cornerstone Science Foundation through the XPLOER PRIZE. D.C. acknowledges support from the Science and Technology Facilities Council (STFC) grant number ST/X001121/1. N.E.R. acknowledges partial support from MIUR, PRIN 2017 (grant 20179ZF5KS). N.E.R., A.P., and S.B. acknowledge the PRIN-INAF 2022 grant “Shedding light on the nature of gap transients: from the observations to the models.” C.S.K. is supported by NSF grants AST-1908570, AST-2307385, and AST-2407206. M.F. is supported by a Royal Society—Science Foundation Ireland University Research Fellowship. P.C. and R.K. acknowledge support via the Research Council of Finland (grant 340613). M.D.S. is funded by the Independent Research Fund Denmark (IRFD, grant No. 10.46540/2032-00022B). J.L.P. acknowledges support from ANID, Millennium Science Initiative, AIM23-0001. L.W. and M.G. acknowledge funding from the European Union’s Horizon 2020 research and innovation program under grant agreement No. 101004719 (OPTICON-RadioNET Pilot, ORP). L.W., M.G., and A.H. acknowledge support from the Polish National Science Centre (NCN) grant No. 2015/17/B/ST9/03167 (OPUS) to L.W., and the Polish participation in SALT is funded by grant No. MNiSW DIR/WK/2016/07. J.M. has the support of the National Key R&D Program of China (2023YFE0101200), the National Natural Science Foundation of China (NSFC 12393813), CSST grant CMS-CSST-2021-A06, and the Yunnan Revitalization Talent Support Program (YunLing Scholar Project). E.R.C. acknowledges support from the National Research Foundation of South Africa. R.D. acknowledges funds by ANID grant FONDECYT Postdoctorado No. 3220449. The Cosmic Dawn Center (DAWN) is funded by the Danish National Research Foundation under grant DNR140.

Based on observations made with the Nordic Optical Telescope, owned in collaboration by the University of Turku and Aarhus University and operated jointly by Aarhus University, the University of Turku, and the University of Oslo, representing Denmark, Finland, and Norway; the University of Iceland; and Stockholm University at the

Observatorio del Roque de los Muchachos, La Palma, Spain, of the Instituto de Astrofísica de Canarias.

Observations from the NOT were obtained through the NUTS collaboration, which is supported in part by the Instrument Centre for Danish Astrophysics (IDA). The data presented here were obtained in part with ALFOSC, which is provided by the Instituto de Astrofísica de Andalucía (IAA) under a joint agreement with the University of Copenhagen and NOTSA.

Based on observations made with the GTC telescope in the Spanish Observatorio del Roque de los Muchachos of the Instituto de Astrofísica de Canarias.

This work is based on observations made with the Large Binocular Telescope. The LBT is an international collaboration among institutions in the United States, Italy, and Germany. LBT Corporation partners are the University of Arizona on behalf of the Arizona Board of Regents; Istituto Nazionale di Astrofísica, Italy; LBT Beteiligungsgesellschaft, Germany, representing the Max-Planck Society, the Leibniz Institute for Astrophysics Potsdam, and Heidelberg University; and the Ohio State University, representing OSU, the University of Notre Dame, the University of Minnesota, and the University of Virginia.

Some of the observations reported in this paper were obtained with the Southern African Large Telescope (SALT) as part of the Large Science Programme on transients 2016-2-LSP-001 (PI: Buckley).

This work has made use of data from the Asteroid Terrestrial-impact Last Alert System (ATLAS) project. The Asteroid Terrestrial-impact Last Alert System (ATLAS) project is primarily funded to search for near-Earth asteroids through NASA grants NN12AR55G, 80NSSC18K0284, and 80NSSC18K1575; by-products of the NEO search include images and catalogs from the survey area. This work was partially funded by Kepler/K2 grant J1944/80NSSC19K0112 and HST GO-15889 and STFC grants ST/T000198/1 and ST/S006109/1. The ATLAS science products have been made possible through the contributions of the University of Hawaii Institute for Astronomy, the Queen's University Belfast, the Space Telescope Science Institute, the South African Astronomical Observatory, and the Millennium Institute of Astrophysics (MAS), Chile.

The Liverpool Telescope is operated on the island of La Palma by Liverpool John Moores University in the Spanish Observatorio del Roque de los Muchachos of the Instituto de Astrofísica de Canarias with financial support from the UK Science and Technology Facilities Council. This work makes use of data from the Las Cumbres Observatory network.

This research uses data obtained through the Telescope Access Program (TAP), which has been funded by the TAP member institutes. We thank the former Swift PI, the late Neil Gehrels, the Observation Duty Scientists, and the science planners for approving and executing our Swift/UVOT program.

This publication makes use of data products from the Wide-field Infrared Survey Explorer, which is a joint project of the University of California, Los Angeles, and the Jet Propulsion Laboratory/California Institute of Technology, funded by the National Aeronautics and Space Administration. This publication also makes use of data products from NEOWISE, which is a project of the Jet Propulsion Laboratory/California Institute of Technology, funded by the Planetary Science Division of the National Aeronautics and Space Administration.

We thank Las Cumbres Observatory and its staff for their continued support of ASAS-SN. ASAS-SN is funded in part by the Gordon and Betty Moore Foundation through grants GBMF5490 and GBMF10501 to the Ohio State University, and also funded in part by the Alfred P. Sloan Foundation grant G-2021-14192.

## Appendix A Observations of CSS 161010

### A.1. Photometry

Multiwavelength photometric coverage of CSS 161010 was acquired between 2016 October 10 and 2016 December 27. During the first 9 days, three epochs of  $V$  photometry were obtained by ASAS-SN; after this, *B<sub>g</sub>V<sub>r</sub>I<sub>z</sub>* optical imaging data were obtained with the 2 m Liverpool Telescope (LT) using the IO:O imager, the 2.56 m Nordic Optical Telescope (NOT) using the Alhambra Faint Object Spectrograph and Camera (ALFOSC) at the Roque de Los Muchachos Observatory (Spain), the 1.0 m telescopes of the Las Cumbres Observatory Global Telescope Network (LCOGT; T. M. Brown et al. 2013), the 2.4 m Hiltner telescope at the MDM Observatory, the 1.04 m Sampurnanad Telescope in the Aryabhata Research Institute of observational sciences, the 1.3 m Devasthal Fast Optical (DFOT; R. Sagar et al. 2012) telescope at Nainital (India), and the imaging modes of the Low Dispersion Survey Spectrograph (LDSS-3) and Inamori Magellan Areal Camera and Spectrograph (IMACS) mounted on the 6.5 m Magellan telescopes. Additionally, seven epochs of NIR  $H$  photometry were obtained with the LT using the IO:I imager, while three epochs of UV optical observations were obtained with the UltraViolet/Optical Telescope (UVOT) on board the Swift spacecraft. There were no X-ray detections associated with these Swift observations, with a  $3\sigma$  Swift XRT upper limit on the 0.5–10 keV flux of  $4 \times 10^{-13}$  erg cm<sup>-2</sup> at 25.14 days and  $8 \times 10^{-14}$  erg cm<sup>-2</sup> at 29.5 days (stacking the data from 25.14, 30.17, and 33.06 days). Here we have assumed a flux distribution that is  $\propto \nu^{-1}$  and a column density of X-ray-absorbing gas consistent with only Milky Way absorption. All NOT observations were obtained through the NOT Unbiased Transient Survey<sup>46</sup> allocated time.

All images were reduced using standard procedures, including bias removal and flat-field correction. For the NIR images, the reductions also included sky subtraction. We used the photometric pipeline *PmPYeasy* (P. Chen et al. 2022) to obtain the optical and NIR photometry. We followed the photometry procedures outlined in P. Chen et al. (2022), which primarily include the following three steps: image registration and source detection, measuring instrumental magnitudes with arbitrary zero-points, and deriving photometric zero-points to put the magnitudes into standard magnitude systems. We performed aperture photometry for all the images using a 5''0 radius circular aperture. We used a relatively large aperture to include the flux of both the transient and the underlying host galaxy of CSS 161010. We used the PS1 DR1 MeanObject database (H. A. Flewelling et al. 2020) for the optical-band photometric calibration. The final  $B$ ,  $V$  magnitudes are in the Vega system, and  $g$ -,  $r$ -,  $i$ -, and  $z$ -band magnitudes are in AB magnitudes. We used the Two Micron All Sky Survey (M. F. Skrutskie et al. 2006) photometric catalog for the NIR

<sup>46</sup> <https://nuts.sn.ie>

**Table A1**  
Optical Photometry of CSS 161010<sup>a</sup>

UT Date	JD	Phase (days) <sup>c</sup>	<i>B</i> (mag)	<i>V</i> (mag)	<i>g</i> (mag)	<i>r</i> (mag)	<i>i</i> (mag)	<i>z</i> (mag)	Telescope/Instrument <sup>b</sup>
20161006	2457667.78	...	...	<17.54 <sup>d</sup>	...	...	...	...	ASAS-SN
20161010	2457671.70	1.72	...	16.52 ± 0.12	...	...	...	...	ASAS-SN
20161012	2457673.85	3.80	...	15.47 ± 0.06	...	...	...	...	ASAS-SN
20161013	2457674.95	4.87	...	15.68 ± 0.07	...	...	...	...	ASAS-SN
20161015	2457676.94	6.79	...	16.45 ± 0.17	...	...	...	...	ASAS-SN
20161018	2457679.59	9.36	...	...	16.75 ± 0.08	16.89 ± 0.11	17.21 ± 0.10	17.14 ± 0.09	LT/IO:O
20161018	2457679.63	9.39	17.02 ± 0.04	16.94 ± 0.05	16.96 ± 0.03	16.95 ± 0.09	17.01 ± 0.09	17.10 ± 0.08	NOT/ALFOSC
20161018	2457680.11	9.86	17.19 ± 0.08	...	...	...	17.31 ± 0.10	...	LCOGT
20161020	2457681.87	11.56	17.56 ± 0.13	17.76 ± 0.17	...	17.99 ± 0.21	17.66 ± 0.25	...	LCOGT
20161021	2457682.57	12.24	...	...	17.65 ± 0.13	17.80 ± 0.06	18.06 ± 0.06	18.20 ± 0.09	LT/IO:O
20161022	2457683.57	13.21	...	...	17.89 ± 0.14	18.00 ± 0.06	18.22 ± 0.10	18.04 ± 0.18	LT/IO:O
20161023	2457684.57	14.17	...	...	18.12 ± 0.13	18.20 ± 0.04	18.50 ± 0.07	18.40 ± 0.10	LT/IO:O
20161026	2457688.39	17.87	19.01 ± 0.14	18.82 ± 0.16	...	...	...	...	LCOGT
20161029	2457691.49	20.87	19.26 ± 0.10	19.29 ± 0.16	...	19.11 ± 0.11	19.23 ± 0.19	...	LCOGT
20161030	2457691.67	21.04	19.40 ± 0.04	19.47 ± 0.08	...	19.38 ± 0.06	19.17 ± 0.11	19.33 ± 0.18	NOT/ALFOSC
20161101	2457693.61	22.92	...	...	19.58 ± 0.15	19.57 ± 0.11	19.82 ± 0.13	19.61 ± 0.18	LT/IO:O
20161102	2457694.52	23.80	...	...	19.62 ± 0.14	19.65 ± 0.06	19.85 ± 0.09	19.65 ± 0.14	LT/IO:O
20161102	2457695.08	24.34	19.94 ± 0.15	19.63 ± 0.17	...	19.81 ± 0.18	20.03 ± 0.37	...	LCOGT
20161105	2457697.50	26.68	19.87 ± 0.16	...	...	20.22 ± 0.26	...	...	LCOGT
20161110	2457702.55	31.57	...	...	20.55 ± 0.21	20.71 ± 0.16	21.04 ± 0.26	20.01 ± 0.13	LT/IO:O
20161110	2457702.76	31.77	20.80 ± 0.14	20.73 ± 0.17	...	20.75 ± 0.12	20.92 ± 0.39	...	LCOGT
20161118	2457710.88	39.63	22.39 ± 0.81	21.49 ± 0.34	...	21.93 ± 0.54	22.17 ± 1.02	...	MDM
20161119	2457711.51	40.24	...	...	22.21 ± 0.38	21.43 ± 0.18	22.06 ± 0.42	21.98 ± 0.56	LT/IO:O
20161120	2457713.49	42.15	...	...	22.45 ± 0.24	21.87 ± 0.10	21.98 ± 0.35	21.19 ± 0.20	LT/IO:O
20161129	2457721.64	50.04	...	...	...	22.55 ± 0.48	...	...	LT/IO:O
20161205	2457727.59	55.80	23.50 ± 0.86	22.42 ± 0.49	24.00 ± 0.67	23.19 ± 0.39	...	...	NOT/ALFOSC
20161210	2457732.57	60.61	...	22.88 ± 0.85	24.99 ± 2.80	22.94 ± 0.48	23.04 ± 0.97	...	NOT/ALFOSC
20161224	2457746.67	74.26	...	...	...	23.97 ± 0.56	...	...	Mag/LDSS-3
20161227	2457749.53	77.02	...	...	...	22.94 ± 0.27	...	22.07 ± 0.38	LT/IO:O
20161227	2457750.45	77.91	...	...	22.24 ± 0.95	...	23.04 ± 0.90	...	LT/IO:O
Host									
20170721	2457955.91	276.69	...	...	21.67 ± 0.04	21.26 ± 0.03	20.97 ± 0.11	20.74 ± 0.08	Mag/LDSS-3
20170919	2457984.87	304.71	22.17 ± 0.23	21.64 ± 0.22	...	...	...	...	Mag/IMACS
20170922	2458018.65	337.39	22.03 ± 0.14	21.44 ± 0.12	21.59 ± 0.26	21.17 ± 0.18	20.84 ± 0.27	20.57 ± 0.24	NOT/ALFOSC

**Notes.**<sup>a</sup> All reported magnitudes are host-subtracted.<sup>b</sup> Telescope code: LCOGT, Las Cumbres Observatory Global Network; LT, 2.0 m Liverpool Telescope; Mag/IMACS, Inamori Magellan Areal Camera and Spectrograph on Magellan; Mag/LDSS-3, the Low Dispersion Survey Spectrograph on Magellan; MDM, Hiltner 2.4 m telescope in the MDM Observatory; NOT/ALFOSC, Alhambra Faint Object Spectrograph and Camera on the NOT. *BV* photometry is in the Vega system; *griz* photometry is in the AB system.<sup>c</sup> Rest-frame phase in days from the start of the outburst, JD = 2457669.92 ± 2.00.<sup>d</sup> 3σ upper limit.

photometric calibration. The NIR magnitudes are in the Vega system. The host galaxy flux was subtracted to get the transient brightness. We used galaxy images obtained with the 6.5 m Magellan telescopes (LDSS-3 and IMACS) on 2017 July 21 and 2017 September 19 to estimate the host galaxy flux.

We used the HEASOFT<sup>47</sup> tool set for Swift UVOT photometry. We first summed the exposures for each epoch using the task `uvotimsum`, and then we extracted source counts from a 5''0 radius region centered on CSS 161010 using the task `uvotsource`. The source counts were converted into the AB magnitude system based on the most recent UVOT calibrations (A. A. Breeveld et al. 2011). The galaxy flux was subtracted to get the Swift UVOT photometry. Optical, UVOT,

and NIR photometry are presented in Tables A1, A2, A3, and A4.

Photometry in the orange (*c*) and cyan (*o*) filters (blue and red filters that cover a wavelength range between 4200 and 6500 Å and from 5600 to 8200 Å, respectively) was obtained by the twin 0.5 m ATLAS (J. L. Tonry et al. 2018; K. W. Smith et al. 2020) and through the ATLAS forced photometry server.<sup>48</sup> Table A5 lists the mean magnitudes.

The host galaxy of CSS 161010 was also imaged by the Wide-field Infrared Survey Explorer (WISE) in multiple epochs before and after its discovery.

We also obtained two epochs of NIR imaging with NOTCam at the NOT on 2017 February 6 (in *H*) and 2017 February 19 (in *JK*). These images were reduced using standard NIR

<sup>47</sup> <https://heasarc.gsfc.nasa.gov/docs/software/heasoft/> v. 6.29c.<sup>48</sup> <https://fallingstar-data.com/forcedphot/>



**Table A2**  
BVRI Photometry Obtained with DFOT in the Vega System

UT Date	JD	Phase (days) <sup>a</sup>	<i>B</i> (mag)	<i>V</i> (mag)	<i>R</i> (mag)	<i>I</i> (mag)
20161022	2457684.29	13.90	18.33 ± 0.07	18.09 ± 0.05	...	17.81 ± 0.11
20161023	2457685.43	15.00	18.55 ± 0.06	18.33 ± 0.04	18.23 ± 0.04	18.02 ± 0.11
20161102	2457695.48	24.73	19.87 ± 0.11	...	...	...
20161108	2457701.22	30.28	...	...	...	19.34 ± 0.22

**Note.**

<sup>a</sup> Rest-frame phase in days from the start of the outburst, JD = 2457669.92 ± 2.00.

**Table A3**  
UV Photometry Obtained with Swift in the AB System<sup>a</sup>

UT Date	JD	Phase (days) <sup>b</sup>	UVW1 (mag)	UVM2 (mag)	UVW2 (mag)
20161103	2457695.90	25.14	20.62 ± 0.24	20.55 ± 0.22	20.60 ± 0.19
20161108	2457701.10	30.17	21.00 ± 0.24	21.18 ± 0.22	21.31 ± 0.21
20161111	2457704.09	33.06	22.44 ± 0.74	21.46 ± 0.31	21.69 ± 0.31

**Notes**

<sup>a</sup> All reported magnitudes are host-subtracted.

<sup>b</sup> Rest-frame phase in days from the start of the outburst, JD = 2457669.92 ± 2.00.

**Table A4**  
*H* Photometry in the Vega System

UT Date	JD	Phase (days) <sup>a</sup>	Magnitude (mag)
20161018	2457679.60	9.37	16.51 ± 0.10
20161021	2457682.58	12.24	16.99 ± 0.08
20161022	2457683.57	13.21	17.21 ± 0.12
20161023	2457684.57	14.17	17.42 ± 0.16
20161029	2457690.61	20.02	17.60 ± 0.18
20161030	2457691.59	20.97	17.60 ± 0.19
20161031	2457692.55	21.89	17.70 ± 0.23

**Note.**

<sup>a</sup> Rest-frame phase in days from the start of the outburst, JD = 2457669.92 ± 2.00.

reduction techniques in the NOTCam package<sup>49</sup> in IRAF. We searched for IR emission from the transient using the NIR images obtained on 2018 November 15 (C20). After alignment and subtraction (C. Alard & R. H. Lupton 1998; C. Alard 2000) between the 2017 and 2018 images, we found no trace of emission from the transient. A bright NIR source near the position of CSS 161010 was detected in the NOTCam images, which is the same source as reported in 2020 (C20). It does not show any significant variability between the two observations.

The bright NIR source is also detected in the WISE satellite in the W1 and W2 bands at 3.6 μm and 4.4 μm, respectively (C20). We queried the unTimely catalog (A. M. Meisner et al. 2023), a time-domain catalog of WISE detections derived from the unWISE coadded images (A. M. Meisner et al. 2018), in order to search for any variability in the source that could indicate transient flux associated with CSS 161010. The mean date of the images obtained by the WISE satellite in the first visit after the first ASAS-SN detection of CSS 161010 was on

<sup>49</sup> <https://www.not.iac.es/instruments/notcam/guide/observe.html>

**Table A5**  
ATLAS AB Optical Photometry

UT Date	JD	Phase (days) <sup>a</sup>	Band	Magnitude (mag)
20161006	2457668.14	...	<i>c</i>	<19.59
20161010	2457672.12	2.13	<i>o</i>	16.36 ± 0.02
20161015	2457677.08	6.93	<i>o</i>	16.38 ± 0.11
20161018	2457681.11	10.82	<i>o</i>	17.39 ± 0.05
20161027	2457689.10	18.56	<i>c</i>	18.85 ± 0.11
20161104	2457697.08	26.28	<i>c</i>	20.22 ± 0.26
20161107	2457700.05	29.15	<i>c</i>	20.16 ± 0.37
20161108	2457701.06	30.13	<i>o</i>	20.27 ± 0.64
20161112	2457705.01	33.95	<i>o</i>	<21.51
20161120	2457713.03	41.71	<i>o</i>	<21.40
20161124	2457717.04	45.59	<i>c</i>	<20.51

**Note.**

<sup>a</sup> Rest-frame phase in days from the start of the outburst, JD = 2457669.92 ± 2.00.

2017 February 17 (JD = 2457801.93; phase = 130 days). The mean W1 Vega magnitude of all 16 individual detections from 2010 to 2020 in the unTimely catalog is 16.73, with a dispersion of  $\sigma = 0.09$  mag. The W1 magnitude of the source in the 2017 February visit is  $16.6 \pm 0.1$  mag, consistent with no variability. The W2 detection of the source is marginal, and it is not detected in most of the individual unWISE coadds, notably in the 2017 February visit. Finally, we performed image subtraction between the unWISE W1 images immediately before and after the transient using the same methods as above and found no residual that would indicate transient flux.

### A.2. Imaging Polarimetry

Observations of CSS 161010 were made on 2016 December 2, during the commissioning of the imaging polarimetric mode of the Robert Stobie Spectrograph (RSS; E. B. Burgh et al. 2003)

**Table A6**  
Spectroscopic Observations of CSS 161010

UT Date	JD	Phase (days) <sup>a</sup>	Range (Å)	Telescope +Instrument	Grism/Grating
20161018	2457679.64	9.40	3280–9320	NOT+ALFOSC	Grism#4
20161019	2457680.67	10.40	3290–9380	NOT+ALFOSC	Grism#4
20161020	2457681.59	11.29	3290–9370	NOT+ALFOSC	Grism#4
20161030	2457691.65	21.02	3280–9320	NOT+ALFOSC	Grism#4
20161031	2457692.66	22.00	3290–9370	NOT+ALFOSC	Grism#4
20161104	2457697.44	26.62	3700–8300	SALT+RSS	PG0300
20161105	2457697.73	26.91	4030–9050	Mag+IMACS	Gri-300-17.5
20161106	2457698.78	27.92	4030–9050	Mag+IMACS	Gri-300-17.5
20161119	2457711.88	40.60	2980–9670	LBT+MODS	G400L/G670L
20161124	2457716.55	45.11	3520–7620	GTC+OSIRIS	R1000B/R1000R
20161206	2457729.58	57.72	5100–10400	GTC+OSIRIS	R1000R
20170125	2457779.48	106.00	4520–7615	GTC+OSIRIS	R1000B

**Note.** Telescope code: GTC, Gran Telescopio Canarias; LBT, Large Binocular Telescope; Mag, 6.5 m Magellan telescope; NOT, Nordic Optical Telescope; SALT, South African Large Telescope.

<sup>a</sup> Rest-frame phase in days from the start of the outburst,  $JD = 2457669.92 \pm 2$ .

at the South African Large Telescope (SALT; D. A. H. Buckley et al. 2006). Observations were made using the PI06645 filter to minimize the polarizing beam splitter’s spectral dispersion property. Four exposures were obtained with the corresponding half-wave plate in positions  $0^\circ$ ,  $45^\circ$ ,  $22.5^\circ$ , and  $67.5^\circ$ . Each exposure produced both the  $e$  and  $o$  beam on the detector, each Half Wave Plate (HWP) with a field of view of  $4' \times 8'$ . Bias subtraction proceeded in the usual fashion using the standard SALT data reduction tools and flat-fielding. The polarized and unpolarized standard stars Vela1 95 and WD 0310–688 were observed during the same month with the same filter to set the HWP’s zero-point and to measure any instrumental polarization. Aperture photometry was performed on all the sufficiently bright point sources in the science  $e$  and  $o$  images, and the corresponding linear polarization was calculated from the extracted fluxes.

### A.3. Spectroscopy

CSS 161010 was observed spectroscopically at 12 epochs spanning phases between 9.4 and 106.0 days from the start of the outburst. The observations were carried out with five different instruments: ALFOSC at the NOT, MODS (R. W. Pogge et al. 2010) mounted on the twin 8.4 m Large Binocular Telescope (LBT) at Mount Graham International Observatory (Arizona, USA), RSS at the SALT, IMACS on the 6.5 m Magellan telescope, and the Optical System for Imaging and low-Intermediate-Resolution Integrated Spectroscopy (OSIRIS) at the 10.4 m Gran Telescopio Canarias (GTC). The log of spectroscopic observations of CSS 161010 is presented in Table A6.

The spectra were reduced using standard IRAF routines (bias subtraction, flat-field correction, 1D extraction, and wavelength calibration) and custom pipelines (e.g., PYSALT, FOSCGUI<sup>50</sup>). The flux calibration was performed using spectra of standard stars obtained during the same night. All spectra are available via the WISEREP<sup>51</sup> repository (O. Yaron & A. Gal-Yam 2012).<sup>52</sup>

<sup>50</sup> <https://sngroup.oapd.inaf.it>

<sup>51</sup> <https://www.wiserep.org/>

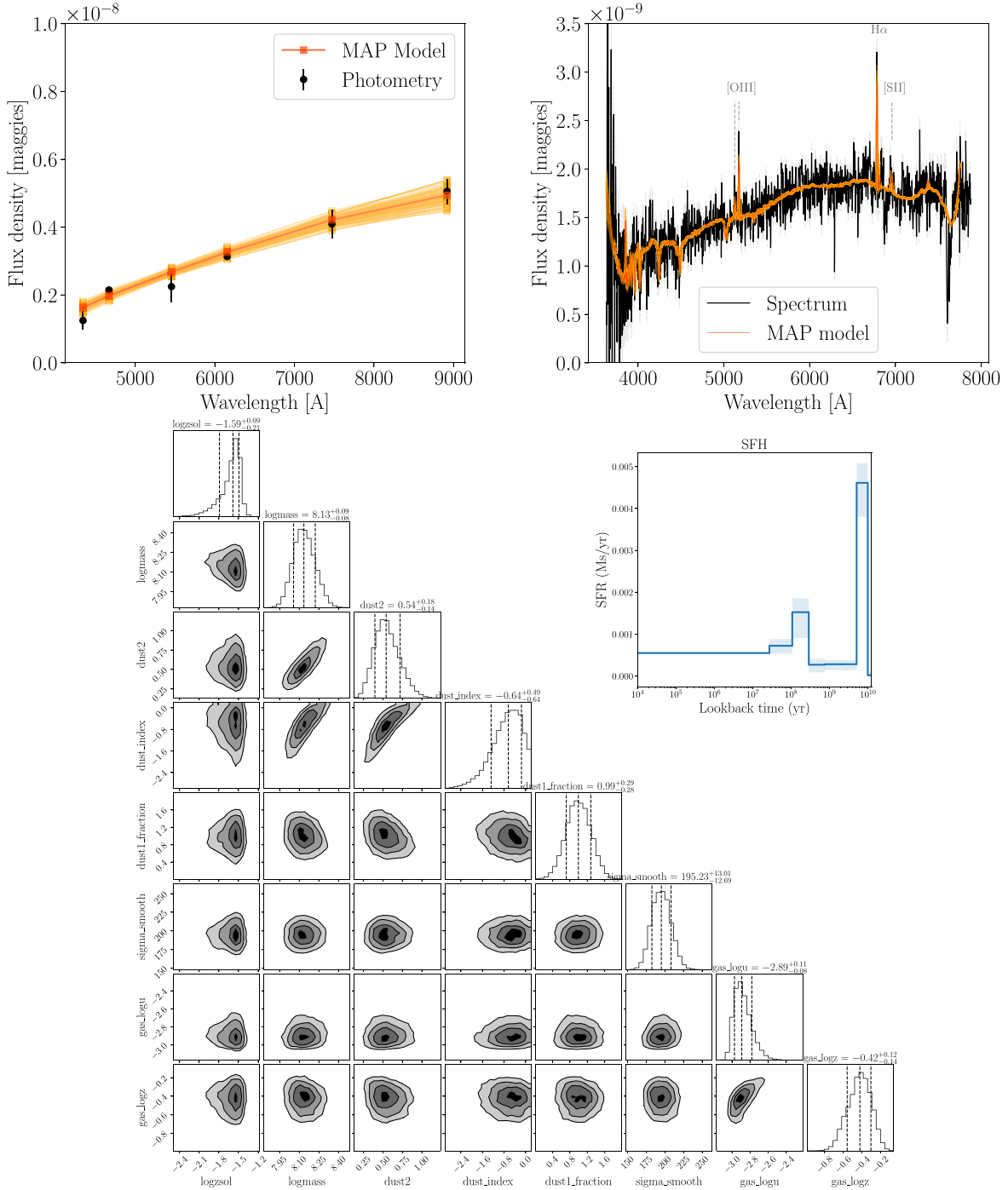
<sup>52</sup> All data (photometry and spectra) are available on Zenodo: doi:10.5281/zenodo.13844163 (in the Supernova data Zenodo Community: <https://zenodo.org/communities/sndata>).

## Appendix B

### Host Galaxy Analysis

Using the host galaxy GTC/OSIRIS spectrum ( $JD = 2457779.48$ ) covering the wavelength range  $3600\text{--}7900\text{ \AA}$  and  $BgVriz$  photometry ( $JD = 2457955.91$  and  $2457984.87$ ), we characterized CSS 161010’s host properties. We use PROSPECTOR (B. D. Johnson et al. 2021), a versatile stellar population fitting tool that uses Monte Carlo sampling of the posterior distributions with EMCEE (D. Foreman-Mackey et al. 2013). The photometry and spectroscopy are simultaneously fit, ensuring a proper spectrum calibration by optimizing the parameters of a polynomial that multiplies the model spectrum to match the observed spectrum at each iteration in the fitting process. Therefore, the spectral continuum does not influence the inferred physical stellar parameters. A free  $\sigma_v$  parameter also ensures that the stellar model spectra are smoothed to the same resolution as the observed spectrum. We use the MILES stellar libraries (P. Sánchez-Blázquez et al. 2006) as provided by the flexible stellar population synthesis code FSPS (C. Conroy et al. 2009; D. Foreman-Mackey et al. 2014) and a nonparametric star formation history consisting of eight age bins. Seven age bins have a free amplitude parameter, while the eighth is constrained by the total stellar mass formed. A single stellar metallicity is inferred, and a dust screen model (M. Kriek & C. Conroy 2013) is assumed to affect all stars and with two free parameters for the dust optical depth  $\tau_V$  and the slope of the attenuation curve. The young stars in star-forming regions ( $<10^7$  yr) are also affected by an additional dust component parameterized by the prescription of L. Blitz & F. H. Shu (1980), including a free gas dust fraction parameter. We also simultaneously fit the nebular part of the spectrum, which has two additional parameters, the gas ionization parameter and the gas-phase metallicity. Thus, we have 15 free parameters inferred through a Monte Carlo sampling with 200 walkers and 2000 iterations. The best-fit models compared to the data, the corner plots of some parameters, and the star formation history are shown in Figure B1. The 16th, 50th, and 84th percentiles of all parameters are shown in Table B1.

The velocity dispersion parameter we obtained,  $\sigma_v = 195.23^{+13.01}_{-12.69}$  km s<sup>-1</sup>, is dominated by the broadening needed



**Figure B1.** Fit results from PROSPECTOR obtained for the photometric SED (upper left) and spectroscopic SED (upper right) of CSS 161010’s galaxy; red lines and points show the best model (maximum a posteriori, or MAP), while the orange lines show 100 random samples of the posterior. The corner plot shows the sampling of the posterior probability distribution for the parameters obtained using PROSPECTOR (excluding the star formation history amplitudes). The middle right plot shows the nonparametric star formation history inferred through eight age bins. The median and 16th and 84th percentiles of CSS 161010’s host parameters are shown in Table B1.

to go from the spectral resolution of the templates to that of the instrument ( $295 \text{ km s}^{-1}$ ). Higher-resolution spectra are necessary for an accurate velocity dispersion that could help constrain the BH mass independently through the  $M$ – $\sigma$  relation (L. Ferrarese & D. Merritt 2000).

We also derived the gas-phase metallicity using the emission lines from the H II region near CSS 161010. By measuring the fluxes of  $\text{H}\alpha$ ,  $\text{H}\beta$ ,  $[\text{O III}] \lambda 5007$ , and  $[\text{N II}] \lambda 6583$  and applying

the O3N2 and N2 diagnostic methods from R. A. Marino et al. (2013) and the diagnostic from M. A. Dopita et al. (2016), we obtained an oxygen abundance of  $12 + \log(\text{O}/\text{H}) = 8.06 \pm 0.05$  dex,  $12 + \log(\text{O}/\text{H}) = 8.22 \pm 0.12$  dex, and  $12 + \log(\text{O}/\text{H}) = 8.03 \pm 0.04$  dex, respectively. These estimates are consistent and suggest a low metallicity ( $0.23 Z_{\odot}$ ), which also agrees quite well with the gas-phase metallicity found with PROSPECTOR ( $0.379^{+0.077}_{-0.118} Z_{\odot}$ ). The difference between the



**Table B1**

Median and 16th and 84th Percentiles of CSS 161010's Host Parameters Obtained with PROSPECTOR

SFR ( $10^{-3} M_{\odot} \text{ yr}^{-1}$ ) at $0.0 < \log(t/\text{yr}) < 7.5$	$0.698^{+0.028}_{-0.052}$
SFR ( $10^{-3} M_{\odot} \text{ yr}^{-1}$ ) at $7.5 < \log(t/\text{yr}) < 8.0$	$0.489^{+0.129}_{-0.193}$
SFR ( $10^{-3} M_{\odot} \text{ yr}^{-1}$ ) at $8.0 < \log(t/\text{yr}) < 8.42$	$1.833^{+0.632}_{-1.089}$
SFR ( $10^{-3} M_{\odot} \text{ yr}^{-1}$ ) at $8.4 < \log(t/\text{yr}) < 8.8$	$0.571^{+0.219}_{-0.238}$
SFR ( $10^{-3} M_{\odot} \text{ yr}^{-1}$ ) at $8.8 < \log(t/\text{yr}) < 9.3$	$0.029^{+0.054}_{-0.022}$
SFR ( $10^{-3} M_{\odot} \text{ yr}^{-1}$ ) at $9.3 < \log(t/\text{yr}) < 9.7$	$0.003^{+0.003}_{-0.002}$
SFR ( $10^{-3} M_{\odot} \text{ yr}^{-1}$ ) at $9.7 < \log(t/\text{yr}) < 10.1$	$0.011^{+0.016}_{-0.007}$
SFR ( $10^{-3} M_{\odot} \text{ yr}^{-1}$ ) at $10.1 < \log(t/\text{yr})^a$	$2.651^{+0.634}_{-1.559}$
$\log(Z/Z_{\odot})$	$-1.586^{+0.092}_{-0.206}$
$\log(M_{*}/M_{\odot})$	$8.135^{+0.087}_{-0.079}$
$\log(\text{age}/\text{yr})^b$	$7.678^{+0.690}_{-0.238}$
Recent SFR ( $M_{\odot} \text{ yr}^{-1}$ )	$0.015^{+0.010}_{-0.008}$
Dust ( $\tau_V$ )	$0.542^{+0.179}_{-0.144}$
Dust index ( $n$ )	$-0.644^{+0.487}_{-0.638}$
Gas dust fraction (%) <sup>c</sup>	$0.994^{+0.288}_{-0.278}$
Gas ionization parameter	$-2.892^{+0.111}_{-0.081}$
$\log(Z_{\text{gas}}/Z_{\odot})$	$-0.421^{+0.118}_{-0.136}$
$\sigma_v$ ( $\text{km s}^{-1}$ )	$195.234^{+13.010}_{-12.693}$

**Notes.**

<sup>a</sup> The last SFR bin is obtained from the other seven bins and the total stellar mass formed.

<sup>b</sup> Mass-weighted age obtained from the total stellar mass and the SFR bins of the star formation history.

<sup>c</sup> Fraction of dust ( $\tau_V$ ) that also affects the young stellar populations ( $< 10^7$  yr).

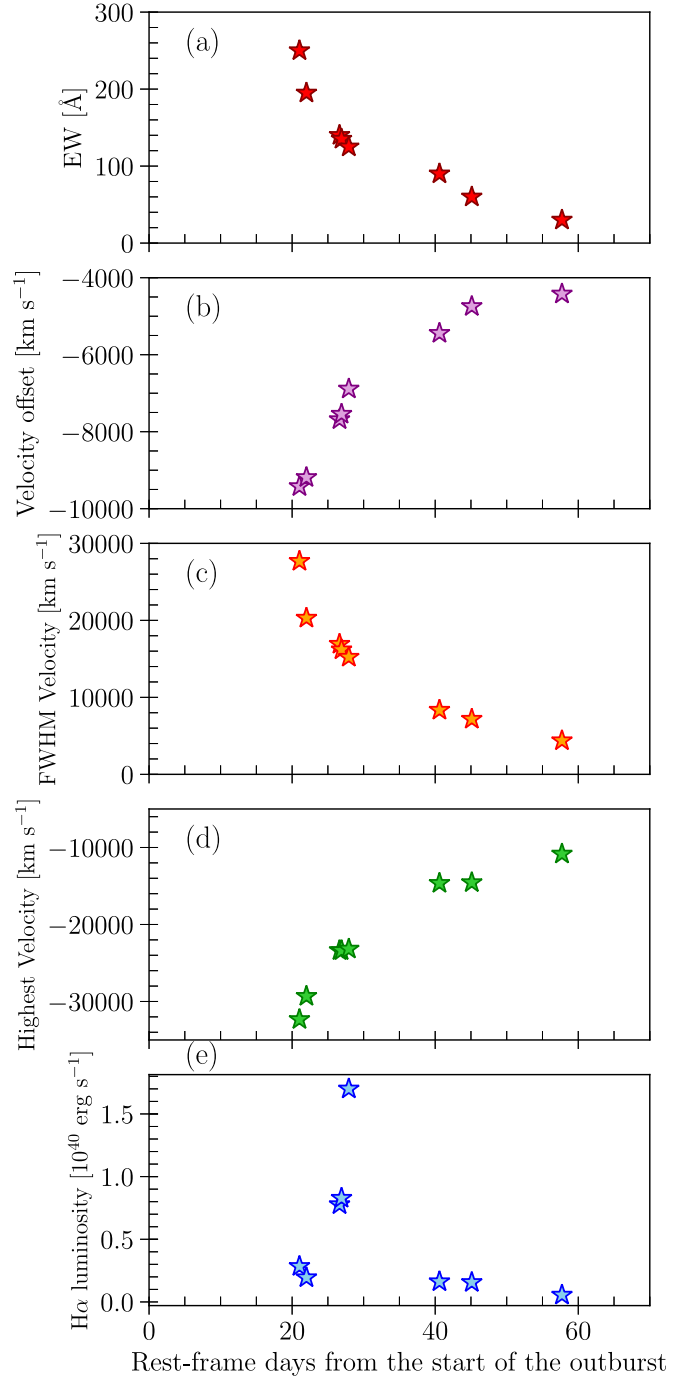
much lower stellar metallicity ( $0.026^{+0.007}_{-0.010} Z_{\odot}$ ) and the gas-phase metallicity could arise from two different star formation episodes in the host galaxy: a very old primordial burst that created most of the old stars with extremely low metallicity and a low but non-null episode of recent star formation that explains the nebular line presence and the higher gas-phase metallicity. This interpretation agrees well with the estimated star formation history that shows two major peaks: one in the oldest bin ( $> 10^{10}$  yr) and a more recent one spanning the youngest four bins ( $< 10^{8.5}$  yr). Similar results have been previously found for other dwarf galaxies (A. Gallazzi et al. 2005; J. Lian et al. 2018; A. Fraser-McKelvie et al. 2022).

A detailed analysis of WISEA J045834.37–081804.4 was presented in 2020 by C20. Using an optical spectrum and photometry, they found a current stellar age of (0.6–4) Gyr, a stellar mass of  $M_{*} \approx 10^7 M_{\odot}$ , an SFR of  $\text{SFR} = 4 \times 10^{-3} M_{\odot} \text{ yr}^{-1}$ , and a specific SFR of  $\text{sSFR} = 0.3 \text{ Gyr}^{-1}$ . They pointed out that their estimated stellar mass would indicate a central BH with an intermediate mass of  $\sim 10^3 M_{\odot}$ , possibly even lower than our estimate. Most of these parameters resemble ours, although the stellar mass differs from our estimations by an order of magnitude. This is mostly due to our addition of z-band photometry that further constrains the stellar mass. However, we noticed that if we run PROSPECTOR with the gas-phase and stellar metallicities fixed to the value found from our host spectrum, we find a stellar mass of  $\log(M_{*}/M_{\odot}) = 7.02^{+0.17}_{-0.14}$ , which is similar to the mass obtained by C20. Nevertheless, we favor our initial result, where the gas-phase and stellar metallicities are free parameters because they provide very different information on the galaxy evolution (A. Fraser-McKelvie et al. 2022).

## Appendix C

### H $\alpha$ Emission Profile Properties

To quantify the evolution of H $\alpha$  in CSS 161010, we measured its equivalent width (EW), velocity offset, full width at half-maximum (FWHM), and highest velocity indicated by the bluest part of the line profile and luminosity (Figure C1). The EW, FWHM, and highest velocity are most affected as the line becomes weaker. The EW evolves from  $\sim 250$  at 21.0 days to  $\sim 30 \text{ \AA}$  at 57.7 days, while the FWHM velocity drops from 28,000 to 4000  $\text{km s}^{-1}$  during the same period. The highest



**Figure C1.** Evolution of the EW (panel (a)), velocity offset (i.e., blueshift of the line peak from the rest wavelength; panel (b)), FWHM velocity (panel (c)), highest velocity (panel (d)), and luminosity (panel (e)) of the H $\alpha$  profile from 21.0 to 57.7 days.

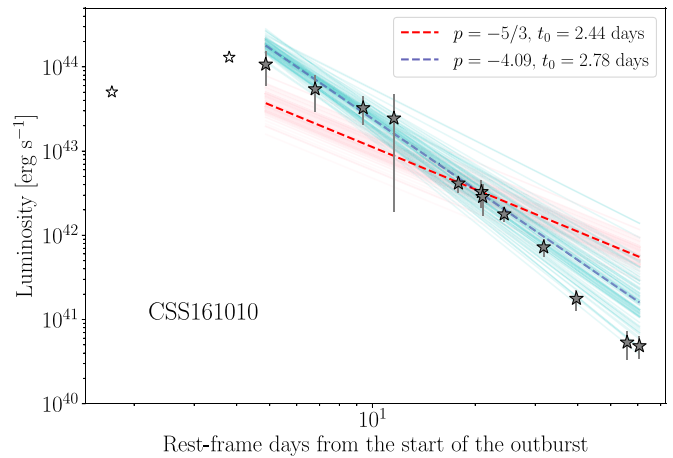
velocities of  $H\alpha$  and  $H\beta$  (the bluest parts of the profile) decrease from  $\sim -33,000 \text{ km s}^{-1}$  at 21.0 days (consistent with the velocities measured for He II) to  $\sim -10,000 \text{ km s}^{-1}$  at 57.7 days, while the line center always remains blueshifted by more than  $-4000 \text{ km s}^{-1}$ . The  $H\alpha$  luminosity rises for  $\sim 8$  days, having a peak luminosity of  $1.67 \times 10^{40}$  at  $\sim 28$  days. Postpeak, the luminosity rapidly decreases, and after  $\sim 40$  days, it has a quasi-constant evolution.

### Appendix D BH Mass from CSS 161010 Light Curve

Recently, evidence has been found that the TDE properties are related to the BH mass (e.g., N. Blagorodnova et al. 2017; T. Wevers et al. 2017; S. van Velzen et al. 2021; E. Hammerstein et al. 2023). This connection is reinforced by a correlation found between the decay rate of the TDE light curve and the BH mass (N. Blagorodnova et al. 2017; S. van Velzen et al. 2019, 2020), where faster-decaying objects have smaller BH masses. Theoretically, the expected decline rate of the postdisruption mass return flow is consistent with a power-law decay  $t^{-5/3}$  (M. J. Rees 1988; E. S. Phinney 1989); however, other parameters can affect it (G. Lodato et al. 2009), and different indices have been found in observations (from  $-0.93$  to  $-2.46$ ; S. van Velzen et al. 2021; E. Hammerstein et al. 2023). In fact, recent simulations have shown that the fallback rate from partial TDEs is proportional to a power-law decay with a  $p$ -index between  $-2$  and  $-5$  (E. R. Coughlin & C. J. Nixon 2019; T. Ryu et al. 2020).

We estimate the  $p$ -index that best reproduces CSS 161010's light curve by fitting a power-law decay ( $L_{\text{bb}} \propto (t/t_0)^p$ ) to its bolometric light curve. We use Monte Carlo sampling of the posterior distributions with EMCEE (D. Foreman-Mackey et al. 2013) to obtain the free parameters in our model, which are the characteristic time ( $t_0$ ) and the power-law index ( $p$ ). We found  $t_0 = 2.78^{+0.28}_{-0.26}$  days and  $p = -4.09 \pm 1.30$  (blue line; Figure D1). This power-law index is the highest reported to date and is in the range of indexes suggested for a partial TDE (T. Ryu et al. 2020).

To constrain the BH mass of a TDE, we can use the correlation between the fallback timescale ( $t_{\text{fb}}$ ) and the BH mass. As  $t_{\text{fb}}$  is comparable to  $t_0$ , we can estimate this parameter by fitting the bolometric light curve of the transient with a power-law decay using a fixed power-law index ( $p = -5/3$ ). With the EMCEE sampler, we fit CSS 161010's bolometric light curve and obtain  $t_0 = 2.44^{+0.29}_{-0.27}$  days (red line; Figure D1). Extrapolating the correlation between  $t_{\text{fb}}$  and BH mass (Figure 8) and using  $t_0 = 2.44$  days, we find a BH mass of  $10^{3.57 \pm 0.10} M_{\odot}$ . For  $t_0 = 2.78^{+0.28}_{-0.26}$  days, we get a BH mass of  $10^{3.67 \pm 0.10} M_{\odot}$ . These BH mass values are in the middle of the range we found using scaling relations (similar to the mass obtained by fitting all galaxies; Figure 1; Appendix B). All

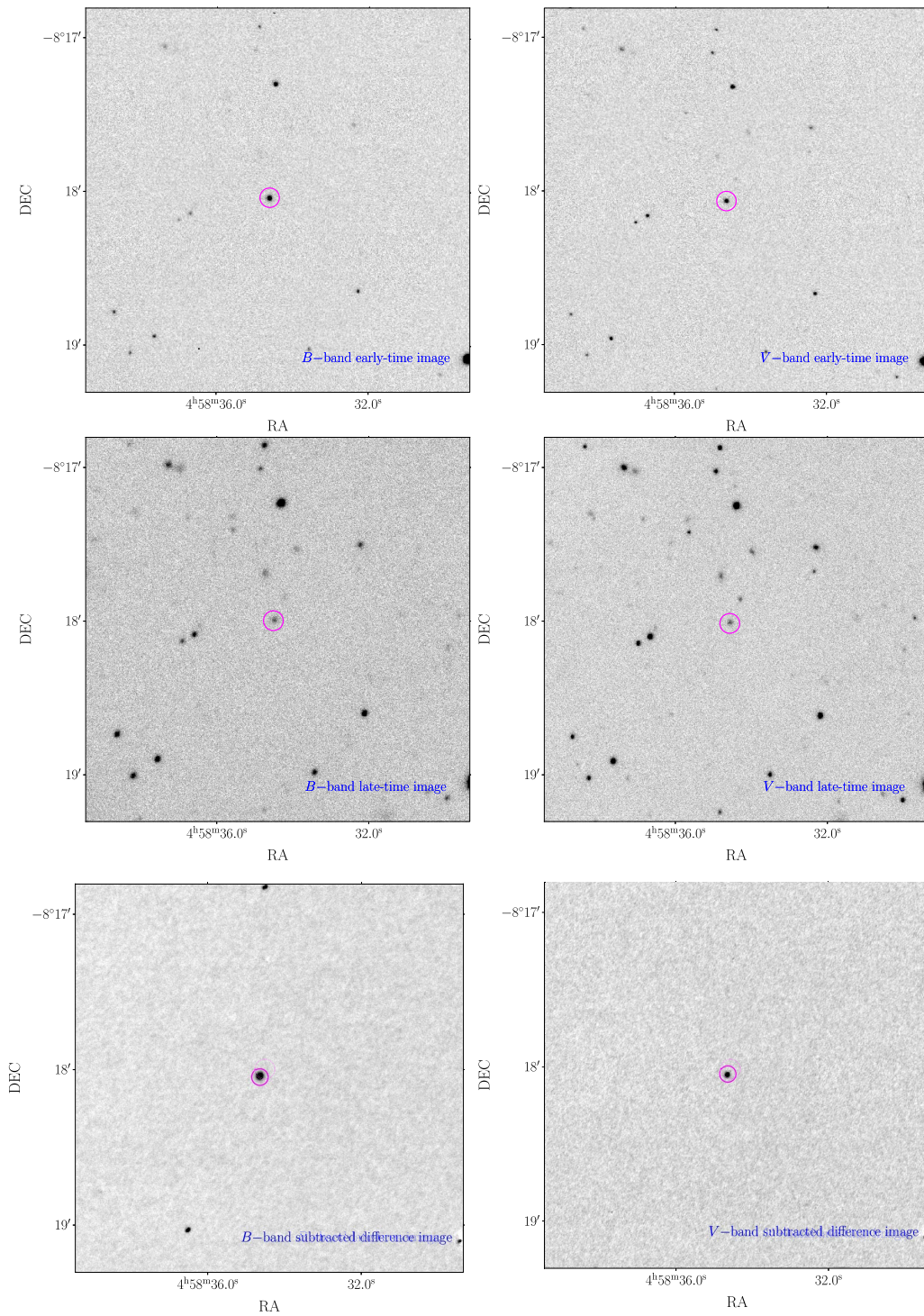


**Figure D1.** Bolometric light curve of CSS 161010. The dashed lines indicated the best fit for  $(t/t_0)^p$  with  $p$  as a free parameter (blue) and  $p = -5/3$  (red). Solid lines (red and blue) show 100 random samples of the posterior by using Markov Chain Monte Carlo.

these findings support CSS 161010 as the fastest-declining TDE (candidate) to date with one of the lowest BH masses.

### Appendix E Location of CSS 161010 within its Host Galaxy

To investigate the location of CSS 161010 within its host galaxy, we selected pairs of images obtained with ALFOSC on the NOT showing the transient while still bright and the host galaxy after the transient had faded away. For this, we used  $B$ - and  $V$ -band images obtained on the nights of 2016 October 29 and 2017 September 21, respectively (Figure E1). The latter images were obtained with a 900 s integration per band. The early-time image in each band was aligned to the late-time image using 10 isolated and nonsaturated stars across the field of view, including shifts in  $x$  and  $y$  and rotation as the free parameters. The early-time images (with a better seeing) were then convolved to match the late-time images using ISIS 2.2 (C. Alard & R. H. Lupton 1998; C. Alard 2000) prior to subtraction. The position of the transient was measured from the subtracted images using centroiding. It was compared with the centroid position of the compact host galaxy measured from the late-time images. We find that in R.A., the transient position coincides with the centroid position of the host galaxy within  $2\sigma$ . However, in decl., we find a statistically significant offset of  $0''.304 \pm 0''.032$  in  $B$  ( $10\sigma$ ) and  $0''.383 \pm 0''.024$  in the  $V$  band ( $16\sigma$ ). At the distance of the host galaxy, the  $V$ -band offset corresponds to a projected distance of 280 pc. In comparison, we measured an FWHM extent of  $1''.7$  (corresponding to 1.2 kpc) for the host galaxy in the late-time  $V$ -band images with a seeing of FWHM =  $1''.1$ . We note that D. L. Coppejans et al. (2020) found a similar offset between the optical and radio coordinates of the transient and its host galaxy in the  $V$  band.



**Figure E1.** Location of CSS 161010 within its host galaxy. Images obtained by ALFOSC on the NOT showing the transient (top), the host galaxy when the transient had faded away (middle), and subtracted difference images (bottom). *B*-band images are shown in the left panels, while *V*-band images are on the right.



## Appendix F Comparison Sample








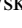
Detailed properties of the comparison sample are presented in Table F1.

**Table F1**  
Detailed Properties of the Comparison Sample

Object	Redshift	Start of the Outburst Date (JD)	References
LBOTS			
AT 2018cow	0.014	2458284.84	S. J. Prentice et al. (2018); D. A. Perley et al. (2019)
AT 2020mrf	0.135	2459012.5	Y. Yao et al. (2022)
AT 2020xnd	0.2433	2459132.50	D. A. Perley et al. (2021); A. Y. Q. Ho et al. (2022)
H-rich SNe			
SN 1979C	0.00455	2443970.5	N. Panagia et al. (1980)
SN 2008es	0.205	2454574.5	S. Gezari et al. (2009)
H-rich TDEs			
AT 2018zr	0.071	2458156.2	T. W. S. Holoien et al. (2019); P. Charalampopoulos et al. (2022)
AT 2020neh	0.062	2459018.6	C. R. Angus et al. (2022)
AT 2020wey	0.0274	2459175.5	P. Charalampopoulos et al. (2023)

### ORCID iDs

Claudia P. Gutiérrez  <https://orcid.org/0000-0003-2375-2064>  
 Seppo Mattila  <https://orcid.org/0000-0001-7497-2994>  
 Peter Lundqvist  <https://orcid.org/0000-0002-3664-8082>  
 Luc Dessart  <https://orcid.org/0000-0003-0599-8407>  
 Santiago González-Gaitán  <https://orcid.org/0000-0001-9541-0317>  
 Peter G. Jonker  <https://orcid.org/0000-0001-5679-0695>  
 Subo Dong  <https://orcid.org/0000-0002-1027-0990>  
 Deanne Coppejans  <https://orcid.org/0000-0001-5126-6237>  
 Panos Charalampopoulos  <https://orcid.org/0000-0002-0326-6715>  
 Nancy Elias-Rosa  <https://orcid.org/0000-0002-1381-9125>  
 Thomas M. Reynolds  <https://orcid.org/0000-0002-1022-6463>  
 Christopher Kochanek  <https://orcid.org/0000-0001-6017-2961>  
 Morgan Fraser  <https://orcid.org/0000-0003-2191-1674>  
 Andrea Pastorello  <https://orcid.org/0000-0002-7259-4624>  
 Mariusz Gromadzki  <https://orcid.org/0000-0002-1650-1518>  
 Jack Neustadt  <https://orcid.org/0000-0001-7351-2531>  
 Stefano Benetti  <https://orcid.org/0000-0002-3256-0016>  
 Erkki Kankare  <https://orcid.org/0000-0001-8257-3512>  
 Tuomas Kangas  <https://orcid.org/0000-0002-5477-0217>  
 Rubina Kotak  <https://orcid.org/0000-0001-5455-3653>  
 Maximilian D. Stritzinger  <https://orcid.org/0000-0002-5571-1833>  
 Thomas Wevers  <https://orcid.org/0000-0002-4043-9400>  
 Bing Zhang  <https://orcid.org/0000-0002-9725-2524>  
 Subhash Bose  <https://orcid.org/0000-0003-3529-3854>  
 David A. H. Buckley  <https://orcid.org/0000-0002-7004-9956>  
 Raya Dastidar  <https://orcid.org/0000-0001-6191-7160>  
 Anjasha Gangopadhyay  <https://orcid.org/0000-0002-3884-5637>  
 Aleksandra Hamanowicz  <https://orcid.org/0000-0002-4646-7509>  
 Jirong Mao  <https://orcid.org/0000-0002-7077-7195>  
 Kuntal Misra  <https://orcid.org/0000-0003-1637-267X>

Stephen. B. Potter  <https://orcid.org/0000-0002-5956-2249>  
 Jose L. Prieto  <https://orcid.org/0000-0003-0943-0026>  
 Encarni Romero-Colmenero  <https://orcid.org/0000-0003-0607-1136>  
 Mridweeka Singh  <https://orcid.org/0000-0001-6706-2749>  
 Auni Somero  <https://orcid.org/0000-0001-6566-9192>  
 Giacomo Terreran  <https://orcid.org/0000-0003-0794-5982>  
 Petri Vaisanen  <https://orcid.org/0000-0001-7673-4850>  
 Łukasz Wyrzykowski  <https://orcid.org/0000-0002-9658-6151>

### References

Abbott, R., Abbott, T. D., Abraham, S., et al. 2020, *ApJL*, 900, L13  
 Alard, C. 2000, *A&AS*, 144, 363  
 Alard, C., & Lupton, R. H. 1998, *ApJ*, 503, 325  
 Anderson, J. P., Dessart, L., Gutiérrez, C. P., et al. 2014, *MNRAS*, 441, 671  
 Andrews, J. E., Gallagher, J. S., Clayton, G. C., et al. 2010, *ApJ*, 715, 541  
 Angus, C. R., Baldassare, V. F., Mockler, B., et al. 2022, *NatAs*, 6, 1452  
 Arcavi, I., Wolf, W. M., Howell, D. A., et al. 2016, *ApJ*, 819, 35  
 Arnett, W. D. 1982, *ApJ*, 253, 785  
 Bellm, E. C., Kulkarni, S. R., Graham, M. J., et al. 2019, *PASP*, 131, 018002  
 Bellovary, J. M., Cleary, C. E., Munshi, F., et al. 2019, *MNRAS*, 482, 2913  
 Blagorodnova, N., Gezari, S., Hung, T., et al. 2017, *ApJ*, 844, 46  
 Blitz, L., & Shu, F. H. 1980, *ApJ*, 238, 148  
 Breeveld, A. A., Landsman, W., Holland, S. T., et al. 2011, in *AIP Conf. Ser.* 1358, *Gamma Ray Bursts 2010*, ed. J. E. McEnery, J. L. Racusin, & N. Gehrels (Melville, NY: AIP), 373  
 Bright, J. S., Margutti, R., Matthews, D., et al. 2022, *ApJ*, 926, 112  
 Brown, T. M., Baliber, N., Bianco, F. B., et al. 2013, *PASP*, 125, 1031  
 Buckley, D. A. H., Swart, G. P., & Meiring, J. G. 2006, *Proc. SPIE*, 6267, 62670Z  
 Burgh, E. B., Nordsieck, K. H., Kobulnicky, H. A., et al. 2003, *Proc. SPIE*, 4841, 1463  
 Burrows, D. N., Kennea, J. A., Ghisellini, G., et al. 2011, *Natur*, 476, 421  
 Charalampopoulos, P., Leloudas, G., Malesani, D. B., et al. 2022, *A&A*, 659, A34  
 Charalampopoulos, P., Pursiainen, M., Leloudas, G., et al. 2023, *A&A*, 673, A95  
 Chen, P., Dong, S., Kochanek, C. S., et al. 2022, *ApJS*, 259, 53  
 Chen, Y., Drout, M. R., Piro, A. L., et al. 2023, *ApJ*, 955, 43  
 Chevalier, R. A., & Fransson, C. 1994, *ApJ*, 420, 268  
 Chrimes, A. A., Coppejans, D. L., Jonker, P. G., et al. 2024a, arXiv:2406.13821  
 Chrimes, A. A., Jonker, P. G., Levan, A. J., et al. 2024b, *MNRAS*, 527, L47  
 Conroy, C., Gunn, J. E., & White, M. 2009, *ApJ*, 699, 486

- Coppejans, D. L., Margutti, R., Terreran, G., et al. 2020, *ApJL*, 895, L23
- Coughlin, E. R., & Nixon, C. J. 2019, *ApJL*, 883, L17
- den Brok, M., Seth, A. C., Barth, A. J., et al. 2015, *ApJ*, 809, 101
- Dessart, L., & Hillier, D. J. 2005, *A&A*, 437, 667
- Donato, D., Cenko, S. B., Covino, S., et al. 2014, *ApJ*, 781, 59
- Dopita, M. A., Kewley, L. J., Sutherland, R. S., & Nicholls, D. C. 2016, *Ap&SS*, 361, 61
- Drake, A. J., et al. 2009, *ApJ*, 696, 870
- Drout, M. R., Chornock, R., Soderberg, A. M., et al. 2014, *ApJ*, 794, 23
- Faris, S., Arcavi, I., Makrygianni, L., et al. 2024, *ApJ*, 969, 104
- Ferrarese, L., & Merritt, D. 2000, *ApJL*, 539, L9
- Flewelling, H. A., Magnier, E. A., Chambers, K. C., et al. 2020, *ApJS*, 251, 7
- Foreman-Mackey, D., Hogg, D. W., Lang, D., & Goodman, J. 2013, *PASP*, 125, 306
- Foreman-Mackey, D., Sick, J., & Johnson, B. 2014, python-fsps: Python bindings to FSPS, v0.1.1, Zenodo, doi:10.5281/zenodo.12157
- Fox, O. D., & Smith, N. 2019, *MNRAS*, 488, 3772
- Fransson, C., Lundqvist, P., & Chevalier, R. A. 1996, *ApJ*, 461, 993
- Fraser-McKelvie, A., Cortese, L., Groves, B., et al. 2022, *MNRAS*, 510, 320
- Gallazzi, A., Charlot, S., Brinchmann, J., White, S. D. M., & Tremonti, C. A. 2005, *MNRAS*, 362, 41
- Gezari, S., Halpern, J. P., Grupe, D., et al. 2009, *ApJ*, 690, 1313
- Graham, M. J., Kulkarni, S. R., Bellm, E. C., et al. 2019, *PASP*, 131, 078001
- Greene, J. E., Strader, J., & Ho, L. C. 2020, *ARA&A*, 58, 257
- Habouzit, M., Volonteri, M., & Dubois, Y. 2017, *MNRAS*, 468, 3935
- Hammerstein, E., van Velzen, S., Gezari, S., et al. 2023, *ApJ*, 942, 9
- He, J. S., Dou, L. M., Ai, Y. L., et al. 2021, *A&A*, 652, A15
- Ho, A. Y. Q., Margalit, B., Bremer, M., et al. 2022, *ApJ*, 932, 116
- Ho, A. Y. Q., Perley, D. A., Chen, P., et al. 2023a, *Natur*, 623, 927
- Ho, A. Y. Q., Perley, D. A., Gal-Yam, A., et al. 2023b, *ApJ*, 949, 120
- Ho, A. Y. Q., Perley, D. A., Kulkarni, S. R., et al. 2020, *ApJ*, 895, 49
- Ho, A. Y. Q., Phinney, E. S., Ravi, V., et al. 2019, *ApJ*, 871, 73
- Holoien, T. W. S., Huber, M. E., Shappee, B. J., et al. 2019, *ApJ*, 880, 120
- Hung, T., Cenko, S. B., Roth, N., et al. 2019, *ApJ*, 879, 119
- Inkenhaag, A., Jonker, P. G., Levan, A. J., et al. 2023, *MNRAS*, 525, 4042
- Inserra, C. 2019, *NatAs*, 3, 697
- Johnson, B. D., Leja, J., Conroy, C., & Speagle, J. S. 2021, *ApJS*, 254, 22
- Kara, E., Miller, J. M., Reynolds, C., & Dai, L. 2016, *Natur*, 535, 388
- Kiroğlu, F., Lombardi, J. C., Kremer, K., et al. 2023, *ApJ*, 948, 89
- Kriek, M., & Conroy, C. 2013, *ApJL*, 775, L16
- Leonard, D. C., Filippenko, A. V., Barth, A. J., & Matheson, T. 2000, *ApJ*, 536, 239
- Lian, J., Thomas, D., Maraston, C., et al. 2018, *MNRAS*, 474, 1143
- Lin, D., Strader, J., Carrasco, E. R., et al. 2018, *NatAs*, 2, 656
- Lipunova, G. V. 1999, *AstL*, 25, 508
- Liu, L.-D., Zhang, B., Wang, L.-J., & Dai, Z.-G. 2018, *ApJL*, 868, L24
- Lodato, G., King, A. R., & Pringle, J. E. 2009, *MNRAS*, 392, 332
- Margutti, R., Metzger, B. D., Chornock, R., et al. 2019, *ApJ*, 872, 18
- Marino, R. A., Rosales-Ortega, F. F., Sánchez, S. F., et al. 2013, *A&A*, 559, A114
- Matthews, D., Margutti, R., Metzger, B. D., et al. 2023, *RNAAS*, 7, 126
- Mattila, S., Pérez-Torres, M., Efstathiou, A., et al. 2018, *Sci*, 361, 482
- Meisner, A. M., Caselden, D., Schlafly, E. F., & Kiwy, F. 2023, *AJ*, 165, 36
- Meisner, A. M., Lang, D., & Schlegel, D. J. 2018, *AJ*, 156, 69
- Metzger, B. D. 2022, *ApJ*, 932, 84
- Mezcua, M. 2017, *IJMPD*, 26, 1730021
- Mezcua, M., Civano, F., Fabbiano, G., Miyaji, T., & Marchesi, S. 2016, *ApJ*, 817, 20
- Migliori, G., Margutti, R., Metzger, B. D., et al. 2024, *ApJL*, 963, L24
- Mummery, A., van Velzen, S., Nathan, E., et al. 2024, *MNRAS*, 527, 2452
- Nguyen, D. D., Seth, A. C., Neumayer, N., et al. 2018, *ApJ*, 858, 118
- Nicholl, M. 2018, *RNAAS*, 2, 230
- Nicholl, M., Wevers, T., Oates, S. R., et al. 2020, *MNRAS*, 499, 482
- Ofek, E. O., Rabinak, I., Neill, J. D., et al. 2010, *ApJ*, 724, 1396
- Osterbrock, D. E., & Ferland, G. J. 2006, *Astrophysics of Gaseous Nebulae and Active Galactic Nuclei* (Sausalito, CA: Univ. Science Books)
- Panagia, N., Vettolani, G., Boksenberg, A., et al. 1980, *MNRAS*, 192, 861
- Pasham, D. R., Ho, W. C. G., Alston, W., et al. 2021, *NatAs*, 6, 249
- Pellegrino, C., Howell, D. A., Vinkó, J., et al. 2022, *ApJ*, 926, 125
- Perley, D. A., Ho, A. Y. Q., Yao, Y., et al. 2021, *MNRAS*, 508, 5138
- Perley, D. A., Mazzali, P. A., Yan, L., et al. 2019, *MNRAS*, 484, 1031
- Phinney, E. S. 1989, in *IAU Symp. 136, The Center of the Galaxy*, ed. M. Morris (Cambridge: Cambridge Univ. Press), 543
- Pogge, R. W., Atwood, B., Brewer, D. F., et al. 2010, *Proc. SPIE*, 7735, 77350A
- Prentice, S. J., Maguire, K., Smartt, S. J., et al. 2018, *ApJL*, 865, L3
- Prentice, S. J., Mazzali, P. A., Pian, E., et al. 2016, *MNRAS*, 458, 2973
- Pursiainen, M., Childress, M., Smith, M., et al. 2018, *MNRAS*, 481, 894
- Rees, M. J. 1984, *ARA&A*, 22, 471
- Rees, M. J. 1988, *Natur*, 333, 523
- Reines, A. E., & Volonteri, M. 2015, *ApJ*, 813, 82
- Rest, A., Garnavich, P. M., Khatami, D., et al. 2018, *NatAs*, 2, 307
- Reynolds, T., Dong, S., Fraser, M., et al. 2016, *ATel*, 9645, 1
- Roth, N., & Kasen, D. 2018, *ApJ*, 855, 54
- Ryu, T., Krolik, J., Piran, T., & Noble, S. C. 2020, *ApJ*, 904, 100
- Sądowski, A., Tejada, E., Gafton, E., Rosswog, S., & Abarca, D. 2016, *MNRAS*, 458, 4250
- Sagar, R., Kumar, B., Omar, A., & Pandey, A. K. 2012, *Proc. SPIE*, 8444, 84441T
- Sánchez-Blázquez, P., Peletier, R. F., Jiménez-Vicente, J., et al. 2006, *MNRAS*, 371, 703
- Schlafly, E. F., & Finkbeiner, D. P. 2011, *ApJ*, 737, 103
- Shakura, N. I., & Sunyaev, R. A. 1973, *A&A*, 24, 337
- Shappee, B. J., Prieto, J. L., Grupe, D., et al. 2014, *ApJ*, 788, 48
- Skrutskie, M. F., Cutri, R. M., Stiening, R., et al. 2006, *AJ*, 131, 1163
- Smith, K. W., Smartt, S. J., Young, D. R., et al. 2020, *PASP*, 132, 085002
- Soker, N. 2022, *RAA*, 22, 055010
- Soker, N., Grichener, A., & Gilkis, A. 2019, *MNRAS*, 484, 4972
- Taddia, F., Stritzinger, M. D., Fransson, C., et al. 2020, *A&A*, 638, A92
- Tonry, J. L., Denneau, L., Heinze, A. N., et al. 2018, *PASP*, 130, 064505
- van Velzen, S., Gezari, S., Hammerstein, E., et al. 2021, *ApJ*, 908, 4
- van Velzen, S., Holoien, T. W. S., Onori, F., Hung, T., & Arcavi, I. 2020, *SSRv*, 216, 124
- van Velzen, S., Stone, N. C., Metzger, B. D., et al. 2019, *ApJ*, 878, 82
- Wen, S., Jonker, P. G., Stone, N. C., & Zabludoff, A. I. 2021, *ApJ*, 918, 46
- Wevers, T., van Velzen, S., Jonker, P. G., et al. 2017, *MNRAS*, 471, 1694
- Wiseman, P., Pursiainen, M., Childress, M., et al. 2020, *MNRAS*, 498, 2575
- Woo, J.-H., Cho, H., Gallo, E., et al. 2019, *NatAs*, 3, 755
- Wu, S., Coughlin, E. R., & Nixon, C. 2018, *MNRAS*, 478, 3016
- Xiang, D., Wang, X., Lin, W., et al. 2021, *ApJ*, 910, 42
- Yao, Y., Ho, A. Y. Q., Medvedev, P., et al. 2022, *ApJ*, 934, 104
- Yaron, O., & Gal-Yam, A. 2012, *PASP*, 124, 668
- Zhang, W., Shu, X., Chen, J.-H., et al. 2022, *RAA*, 22, 125016
- Zuo, W., Guo, H., Sun, J., et al. 2024, *ApJ*, 974, 288